Seismic imaging of the Ecuadorian forearc and arc from joint ambient noise, local, and teleseismic tomography: catching the Nazca slab in the act of flattening

E.E. Rodríguez [1,*] S.L. Beck,[1] A. Meltzer,[2] M. Segovia,[3] M. Ruíz,[3] S. Hernández,[3] S. Roecker [4] C. Lynner [5] C. Koch [6] M.C. Hoskins,[2] P. Charvis,[7] H. Agurto-Detzel,[8] A. Rietbrock[8] and S. León-Ríos[9]

[1]*Department of Geosciences, University of Arizona, 1040 E. 4th St., Tucson, AZ 85721, USA. E-mail: emily.e.rodriguez1@gmail.com*
[2]*Department of Earth and Environmental Sciences Lehigh University, 9A STEPS Bldg. 1 W. Packer Ave., Bethlehem, PA 18015, USA*
[3]*Instituto Geofísico at the Escuela Politécnica Nacional, Av. Ladrón de Guevara E11-253, Quito 170525, Ecuador*
[4] *Earth and Environmental Sciences, Rensselaer Polytechnic Institute, 110 Eighth Street, Troy, NY 12180, USA*
[5]*Department of Earth Sciences, University of Delaware, Newark, DE 19716, USA*
[6]*Sandia National Laboratory, Albuquerque, NM 87185, USA*
[7]*Université Côte d'Azur, IRD, CNRS, Observatoire de la Côte d'Azur, Géoazur, F-06304 Valbonne, France*
[8]*Geophysical Institute (GPI), Karlsruhe Institute of Technology, D-76187 Karlsruhe, Germany*
[9]*Advanced Mining Technology Center, Universidad de Chile, Santiago, Chile*

SUMMARY

The Ecuadorian Andes are a complex region characterized by accreted oceanic terranes driven by the ongoing subduction of the oceanic Nazca plate beneath South America. Present-day tectonics in Ecuador are linked to the downgoing plate geometry featuring the subduction of the aseismic, oceanic Carnegie Ridge, which is currently entering the trench. Using seismic tomography, we jointly invert arrival times of P and S waves from local and teleseismic earthquakes with surface wave dispersion curves to image the structure of the forearc and magmatic arc of the Ecuadorian Andes. Our data set includes > 100 000 traveltimes recorded at 294 stations across Ecuador. Our images show the basement of the central forearc is composed of accreted oceanic terranes with high elastic wave speeds. Inboard of the Carnegie Ridge, the westernmost forearc and coastal cordilleras display relatively low V_p and V_s and high V_p/V_s values, which we attribute to the increased hydration and fracturing of the overriding plate due to the subduction of the thick oceanic crust of the Carnegie Ridge. We additionally image across-arc differences in magmatic architecture. The frontal volcanic arc overlies accreted terranes and is characterized by low velocities and high V_p/V_s indicative of partial melt reservoirs which are limited to the upper crust. In contrast, the main arc displays regions of partial melt across a wider range of depths. The Subandean zone of Ecuador has two active volcanoes built on continental crust suggesting the arc is expanding eastwards. The mid to lower crust does not show indications of being modified from the magmatic process. We infer that the slab is in the process of flattening as a consequence of early-stage subduction of the buoyant Carnegie Ridge.

Key words: Composition and structure of the continental crust; South America; Seismic tomography; Continental margins: convergent; Crustal structure; Subduction zone processes.

1 INTRODUCTION

The Ecuadorian Andes mark the northern extension of the South America subduction zone, characterized by the eastward subduction of the Nazca plate beneath the South American continent with a convergence rate of ∼5–6 cm yr^{-1} (Fig. 1; Trenkamp *et al.* 2002; Kendrick *et al.* 2003; Nocquet *et al.* 2014). The Northern Andes are distinct from their southern continuation by the presence of several oceanic terranes which were accreted onto the South American margin during the Late Paleocene to Eocene (Fig. 1; e.g. Jaillard
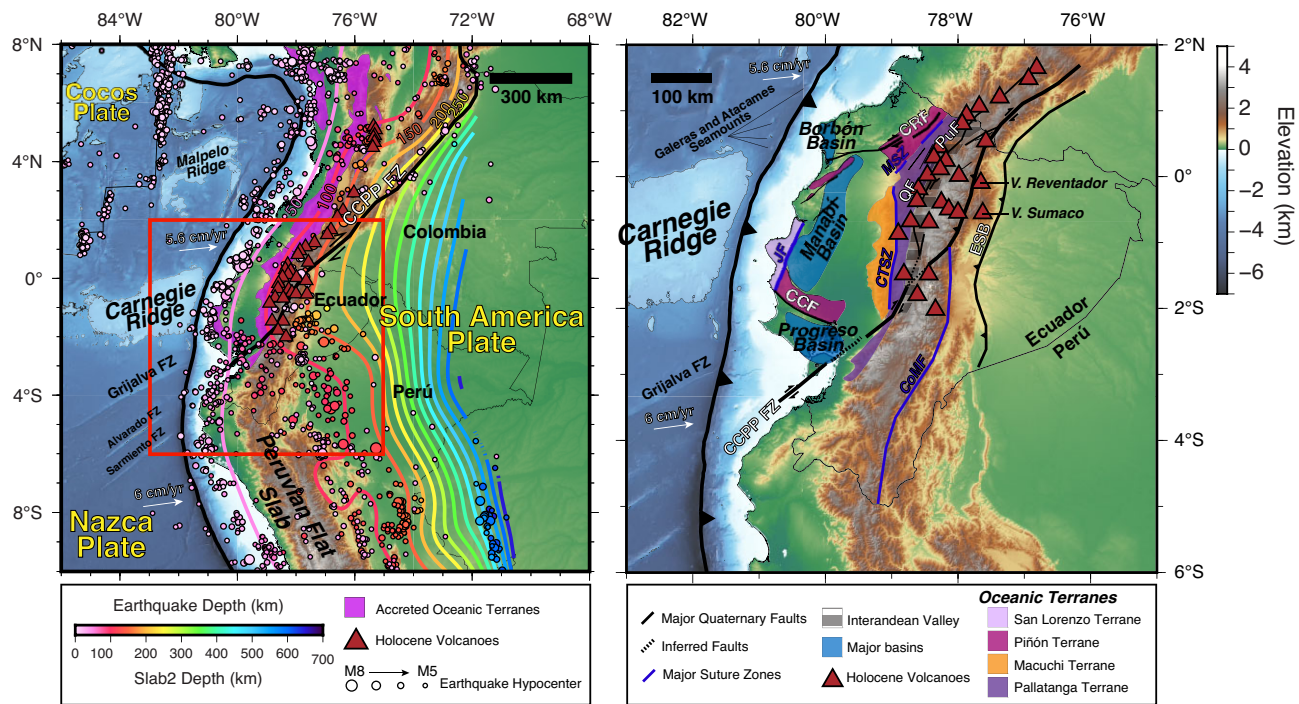
Figure 1. Left: Generalized tectonic map of the Northern Andes. Plotted as circles are >M5 earthquakes from the NEIC catalogue (2023), depths are denoted by the fill colour (see legend). Contours of the top of the Nazca Slab depth are plotted (see legend). Plate convergence direction is shown as arrows relative to South America from Nocquet *et al.* (2014). The purple polygon outlines mapped outcrops of accreted oceanic terranes (Cardona *et al.* 2011). Major bathymetric features are outlined in white. CCPP FZ: Chingual-Cosanga-Pallatanga-Puña Fault Zone; NAS: Northern Andean Sliver. Right: tectonic map adapted from Jaillard *et al.* (2009) and Alvarado *et al.* (2016). Major tectonic regions and faults are highlighted. Red triangles—Holocene Volcanos. Active faults are shown in black and major fault systems are labelled in white text: CCPP FZ: Chingual-Cosanga-Pallatanga-Puná Fault System; CCF: Chongón-Colonche Fault System; CRF: Cañande-Río Lachas Fault System; PuF: Pujili Fault System; QF: Quito Fault System; ESB: Eastern Subandean Belt. Abandoned suture zones are labelled in blue: JF: Jama Fault; MSZ: Mulaute Shear Zone; CTSZ: Chimbo-Toachi Shear Zone; CoMF: Cosanga-Méndez Fault. Back-arc volcanoes, Reventador and Sumaco, are abbreviated as V. Reventador and V. Sumaco, respectively.

et al. 2009; Vallejo *et al.* 2019). These terranes form the basement of the forearc and parts of the Western Cordillera and are described as remnants of an oceanic plateau(s) and volcanic arc(s) (e.g. Kerr *et al.* 2002; Jaillard *et al.* 2009).

The downgoing Nazca slab is between 9 and 30 Ma at the trench and contains the Carnegie Ridge, a large oceanic plateau with thick oceanic crust (15–19 km) that formed at the Galapagos hotspot (Graindorge *et al.* 2004: Gailler *et al.* 2007). Unlike the near horizontal, flat slab subduction of the Nazca Ridge in southern Perú, the Nazca slab inboard of the Carnegie Ridge (CR) in Ecuador has a normal dip as evidenced by the active magmatic arc (Fig. 1). Much debate exists about when the CR began subducting beneath Ecuador, but clearly the magmatic arc has not shut off and the sparse seismicity of the Nazca slab shows a ~20°–30° dipping Wadati–Benioff zone between ~50 and 120 km depth (Fig. 1; e.g. Guillier *et al.* 2001; Font *et al.* 2013; Yepes *et al.* 2016; Araujo *et al.* 2021). Additionally, the Ecuador subduction zone is the site of several >M.7.5 megathrust events over the last 150 yr. No megathrust events have propagated south of the CR, leading many to speculate if the CR is a barrier to propagation (Collot *et al.* 2004; Gailler *et al.* 2007; León-Ríos *et al.* 2019; Koch *et al.* 2020; Lynner *et al.* 2020; León-Ríos *et al.* 2021).

The Ecuadorian margin is an ideal place to study ridge subduction and its influence on the overriding plate, tectonism and magmatism in subduction zones. In this study, we present the results of a joint tomographic inversion of earthquake traveltimes (local and teleseismic) and ambient noise dispersion that illuminate the structure of

the Ecuadorian forearc and magmatic arc. Our images provide clues to the deeper crustal structure of both the accreted terranes and the volcanic arc which may provide insight into the present-day role of the CR.

1.1 Tectonic setting

Presently, the Ecuadorian Andes are characterized by two north–south trending ranges, the Western and Eastern Cordilleras (Fig. 2). The width of the Ecuadorian Andes is ~150–200 km with an average elevation of ~4.5–5 km. These ranges are separated by a topographic depression, the Interandean Valley, and are heavily faulted by several major north–south trending faults (Fig. 1B). The largest of these faults is the Chingual–Cosanga–Pallatanga–Puná (CCPP) Fault System, a transpressive dextral fault, which extends from the Gulf of Guayaquil northward into Colombia on the east side of the Eastern Cordillera (Fig. 1). The CCPP separates the Northern Andean Sliver from continental South America and likely became active ~3 Ma (Witt *et al.* 2006; Alvarado *et al.* 2016). Flanking the cordilleras are the forearc and foreland to the west and east, respectively. The Ecuadorian foreland is further separated into the Subandean Zone, the active portion of the fold and thrust belt and the Basin Oriente (Fig. 2).

The basement of the forearc of Ecuador is thought to largely be comprised of mafic material related to several terranes of oceanic plateau and island arc affinity accreted on to the continent (e.g.
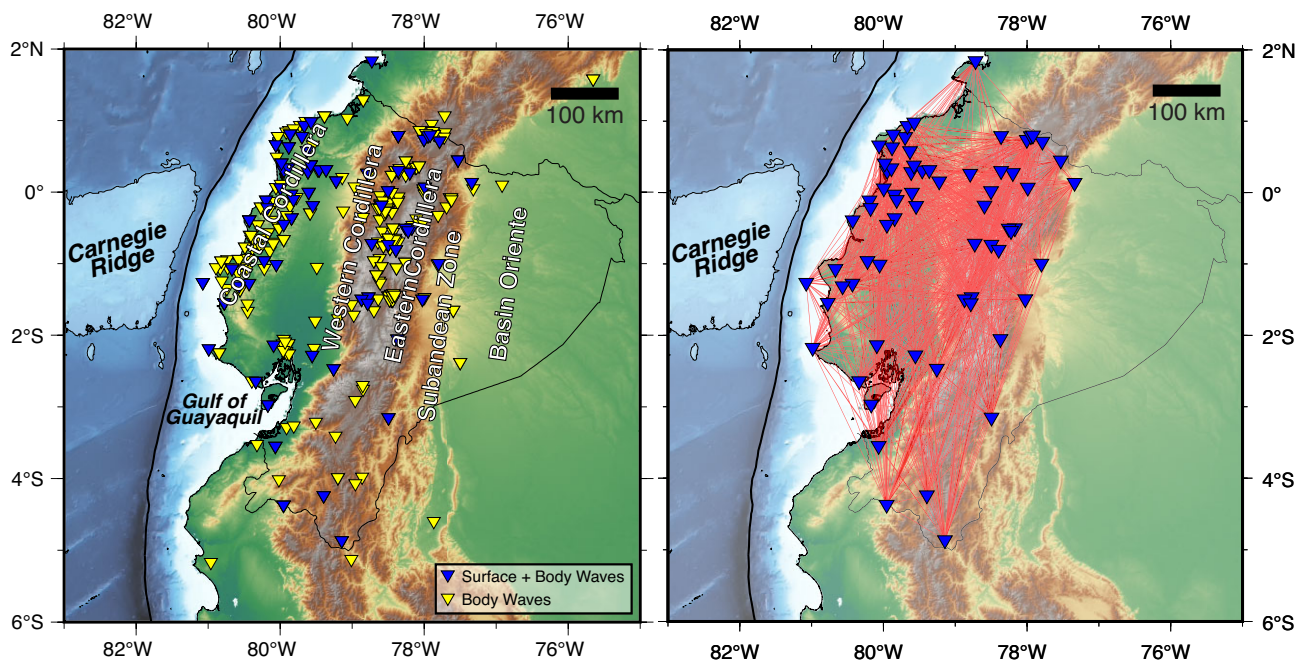
Figure 2. Map of stations used in this study. Left: Inverted triangles denote the location of stations used in this study which recorded body waves and surface wave arrivals. Right: Inverted triangles denote the location of stations used in this study which recorded surface wave arrivals. Interstation paths for data used in our models are shown as red lines.

Jaillard *et al.* 2009). The major terranes along the Ecuadorian margin from east to west include the Pallatanga, Macuchi, Piñón and San Lorenzo terranes, which reside beneath the Interandean Valley, Western Cordillera and Forearc (Fig. 1B; Jaillard *et al.* 2009). While several competing models have been proposed for their timing and formation (e.g. Kerr *et al.* 2002; Jaillard *et al.* 2009; Vallejo *et al.* 2019), these terranes likely accreted to the margin between the Late Cretaceous and Early Eocene.

The easternmost terrane, the Pallatanga terrane (Fig. 1B), is situated along the Western Cordillera and is bounded to the east by the active volcanic arc. The terrane is characterized by a mafic to ultramafic composition, primarily consisting of basalts, peridotites and gabbros (McCourt *et al.* 1998; Kerr *et al.* 2002). Geochemical signatures link the Pallatanga basalts to the Caribbean Oceanic Plateau (COP), indicating the partial accretion of the plateau to the western edge of South America as it migrated northeastward (e.g. Kerr *et al.* 2002). West of the Pallatanga terrane is the Macuchi terrane, also known as the Macuchi Island Arc, separated from the Pallatanga terrane by the Chimbo-Toachi and Mulaute shear zones (Fig. 1B; Hughes & Pilatasig 2002). Comprising volcanic and volcaniclastic rocks, the Macuchi terrane's origin is debated, but it likely represents an island arc accreted to the continent between the Middle Eocene and Late Cretaceous (e.g. Hughes & Pilatasig 2002; Kerr *et al.* 2002; Mamberti *et al.* 2003; Jaillard *et al.* 2009).

Farther west, the Ecuadorian forearc includes the Piñón and San Lorenzo terranes, with the Piñón terrane (Fig. 1B) being the more extensive of the two. It is characterized by a mafic–ultramafic composition, mainly consisting of basalts with small gabbroic intrusions (Kerr *et al.* 2002; Jaillard *et al.* 2009). The Piñón basalts share similarities with the COP in age and geochemical signatures (Hughes & Pilatasig 2002; Mamberti *et al.* 2003; Jaillard *et al.* 2009). The San Lorenzo terrane, the westernmost in Ecuador, is comprised of basalts overlaying the Piñón terrane (Kerr *et al.* 2002). While

some classify it as part of the Piñón terrane, distinctions based on geochemistry suggest an oceanic island arc affinity rather than an oceanic plateau (Kerr *et al.* 2002; Lebrat *et al.* 1987). The exact location of these terranes at the surface is heavily obscured by the Borbón and Manabí sedimentary basins (Fig. 1B) which are estimated to be ~1 and ~4–5 km thick (e.g. Aizprua *et al.* 2020; León-Ríos *et al.* 2021), respectively. Prior seismic studies of the Ecuadorian forearc reveal fast shear-wave velocities through most of the crust that have been attributed to the presence of these mafic terranes throughout much of the forearc basement (Koch *et al.* 2020; Lynner et al., 2020).

The Northern Volcanic Arc of the Andes begins at 2°S in Ecuador and extends northward into Colombia. South of 2°S, the arc is presently inactive due to presence of the Peruvian flat slab (e.g. Gutscher *et al.* 2000; Rosenbaum *et al.* 2019). The volcanic arc in Ecuador is distinctly broad, ~150 km wide, and crosses through the Western Cordillera, Interandean Valley, Eastern Cordillera and into the Subandean zone. The Ecuadorian arc formed ~31–26 Ma and was characterized by small-scale, magmatic episodes until ~6–5 Ma (Hall & Beate 1991). At 6–5 Ma, volcanism increased to produce the modern volcanic front which initiated in the north and migrated southwards (Schütte *et al.* 2010; Bablon *et al.* 2019). The volcanoes at the southern termination of the arc and backarc Subandean zone are the youngest of the modern arc, <600 ka (e.g. Bablon *et al.* 2019). The arc compositions are mainly calc-alkaline andesites and dacites, with some small-volume alkaline compositions in the backarc (e.g. Hall *et al.* 2008; Hidalgo *et al.* 2012; Ancellin *et al.* 2017).

1.2 Subduction of the Nazca plate

The Nazca plate along the margin of Ecuador is notably distinct in its relatively high bathymetry and young age along the margin (~30–9 Ma; e.g. Seton *et al.* 2020). A prominent feature on the

Nazca plate is the Carnegie Ridge (CR), an aseismic oceanic ridge, which currently resides at the trench between 1°N and 2°S and is 2 km shallower than the adjacent seafloor (Fig. 1). The ridge was formed at the Galapagos hotspot and is composed of anomalously thick oceanic crust, estimated to be ~15–19 km thick (Sallarès & Charvis 2003; Graindorge *et al.* 2004; Gailler *et al.* 2007). The time when the CR began subducting is contentious, with estimates ranging from 1.4 to 15 Ma (e.g. Gutscher *et al.* 1999; Spikings & Crowhurst 2004; Lonsdale 2005; Michaud *et al.* 2009; Spikings *et al.* 2010; George *et al.* 2021; Margirier *et al.* 2023). Along the northern edge of the CR are the Atacames and Galeras seamount chains which have been suggested to locally influence plate coupling and seismicity (Fig. 1B; e.g. Font *et al.* 2013; Chlieh *et al.* 2014; Agurto-Detzel *et al.* 2019; León-Ríos *et al.* 2019; Meltzer *et al.* 2019; Soto-Cordero *et al.* 2020; Hoskins *et al.* 2021; León-Ríos *et al.* 2021).

Across the Ecuadorian margin, the downgoing Nazca slab morphology changes significantly from south to north (Fig. 1; Yepes *et al.* 2016; Araujo *et al.* 2021; Rodríguez *et al.* 2024). In the south, starting at ~2.5°S, the slab is currently subducting at a relatively shallow angle and depth of ~100 km for >500 km from the trench, reflecting the north edge of Peruvian flat slab region. North of ~2.5°S the slab resumes a more normal angle of subduction (~20°–45°) along the northern extension of the margin where the modern volcanic arc is active, corresponding to the beginning of the Northern Andean Volcanic Zone (e.g. Guillier *et al.* 2001; Yepes *et al.* 2016; Araujo *et al.* 2021). Beneath the volcanic arc and central Ecuador, intermediate depth seismicity disappears below ~120 km depth, with very few earthquakes recorded within the slab (Fig. 1A; Gutscher *et al.* 1999; Guillier *et al.* 2001; Yepes *et al.* 2016; Araujo *et al.* 2021; NEIC 2023). Limited intermediate-depth slab-seismicity beneath central Ecuador has made it difficult to discern the geometry of the downgoing Nazca plate below ~120 km depth. However, seismic and tomographic studies have shown that the slab dip is relatively steep (20°–30°) beneath central Ecuador (Guillier *et al.* 2001; Yepes *et al.* 2016; Portner *et al.* 2020; Araujo *et al.* 2021; Rodríguez *et al.* 2021; Rodríguez *et al.* 2024).

2 DATA

Seismic body wave data were recorded at 294 stations across Ecuador and southern Colombia from the Ecuador national network (Fig. 2; RENSIG; Ruiz 2016; Alvarado *et al.* 2018), Red Sismológica Nacional de Colombia (Servicio Geológico Colombiano 1993) and temporary station deployments (Régnier *et al.* 2016; Meltzer *et al.* 2019). Our initial local earthquake data set, which were picked analysts at the Instituto Geofísico—Escuela Politécnica Nacional (IG-EPN), includes 390 648 *P*-wave arrivals and 83 272 *S*-wave arrivals recorded from 34 949 unique events during 2014–2020. Potential arrival time outliers were removed using Wadati diagram analysis of each event. This consists of plotting the *P*-wave arrival time verses the S–P time and identifying outliers that indicate unreasonable V_p/V_s ratios. Events selected for analysis were required to have <180° azimuthal gap, at least four station *P*- and two *S*-wave arrivals. Arrivals with travel-time residuals greater than 0.7 s are removed at each stage of the inversion.

We additionally incorporate 34 518 teleseismic *P*-wave arrivals from 1 290 > 5.0 M events and 2 763 teleseismic *S*-wave arrivals from 90 events recorded at 133 stations in Ecuador from 2016 to 2022 (NEIC 2023). The large discrepancy in teleseismic *S*-wave arrival times is due to limited data availability. Teleseismic traveltimes were picked using a multichannel cross-correlation method (Van-Decar & Crosson 1990; Pavlis & Vernon 2010). These events had at least five associated traveltimes with relative residuals of <1.5 s. The final data set for body-wave traveltimes includes data from 5141 local events (79 972 *P*-wave arrivals and 17 931 *S*-wave arrivals; Figs 3 and S1) and 736 teleseismic events (17 682 *P*-wave arrivals and 521 *S*-wave arrivals) at 294 stations which met our quality-control criteria (Fig. 2).

Lastly, we incorporate ambient noise Rayleigh wave traveltimes from Lynner *et al.* (2020). This data set includes 8832 phase-delays from 67 stations recorded in a period range of 6–50 s (Fig. 2). We refer to Lynner *et al.* (2020, and references therein) for descriptions of processing the ambient noise data. The data set includes phase delay measurements from over 5800 interstation paths across 14 periods (6, 8, 10, 12, 14, 16, 18, 20, 25, 30, 35, 40, 45 and 50 s; Fig. 2). We note that measurements at periods less than 10 s and greater than 40 s account for only 8 per cent and 4 per cent, respectively, of the data set.

3 JOINT TOMOGRAPHIC INVERSION

We invert for local earthquake locations and seismic velocity structure using the Joint Tomography Software Package (JTSP) of Roecker *et al.* (2004, 2006). This method simultaneously fits local and teleseismic body-wave traveltimes and surface wave delay times to jointly invert for *P*-wave velocity and V_p/V_s. The inclusion of surface waves in our joint inversion model increases resolution of the crust where we have fewer-to-no ray paths from body waves, particularly in the basins between the Coastal and Western Cordillera (Fig. 2A; Supplementary Fig. S2). Incorporating velocity measurements from surface waves also reduces data uncertainty that might arise from errors in picking *S*-wave arrival times.

JTSP uses a linearized approach to iteratively solve for perturbations to P slowness (U_p) and V_p/V_s (U_s/U_p). Predicted body-wave traveltimes are solved for using a spherical coordinate 3-D eikonal equation solver (Li *et al.* 2009; Zhang *et al.* 2012). Perturbations to P slowness and V_p/V_s are solved for linearly using the partial derivatives for each observation calculated along ray paths (Roecker *et al.* 2004; Comte *et al.* 2016). Surface wave data are incorporated using phase delay times at given frequencies, assuming that the 3-D model can be constructed by combining 1-D models at each model grid point (Montagner, 1986). These delay times are calculated by relating derivatives of shear wave slowness U_s with respect to phase velocity along interstation paths. The partial derivatives of phase velocity with respect to shear wave slowness (U_s) are then used to compute the sensitivity. Perturbations to S slowness are solved for using $\Delta U_s = \Delta(rU_p) = U_p\Delta r + r\Delta U_p$, where $r = U_s/U_p$. This system of linear equations is solved iteratively using the LSQR algorithm (Paige and Saunders, 1982). A full description of the joint inversion methodology can be found in Nunn *et al.* (2014), Comte *et al.* (2016) and Roecker *et al.* (2017).

At each iteration, the model is constrained by a maximum allowed per cent change in wave speed. Local earthquake hypocentres are included as variables in the inversion and are relocated before the next iteration. The entire data set is then re-evaluated to ensure it meets quality control criteria (e.g. the updated velocity model may improve data fit enough to satisfy residual thresholds). Consequently, as the model improves, more data may be included. Our final model was produced after 12 iterations, at which point the RMS of our inverted
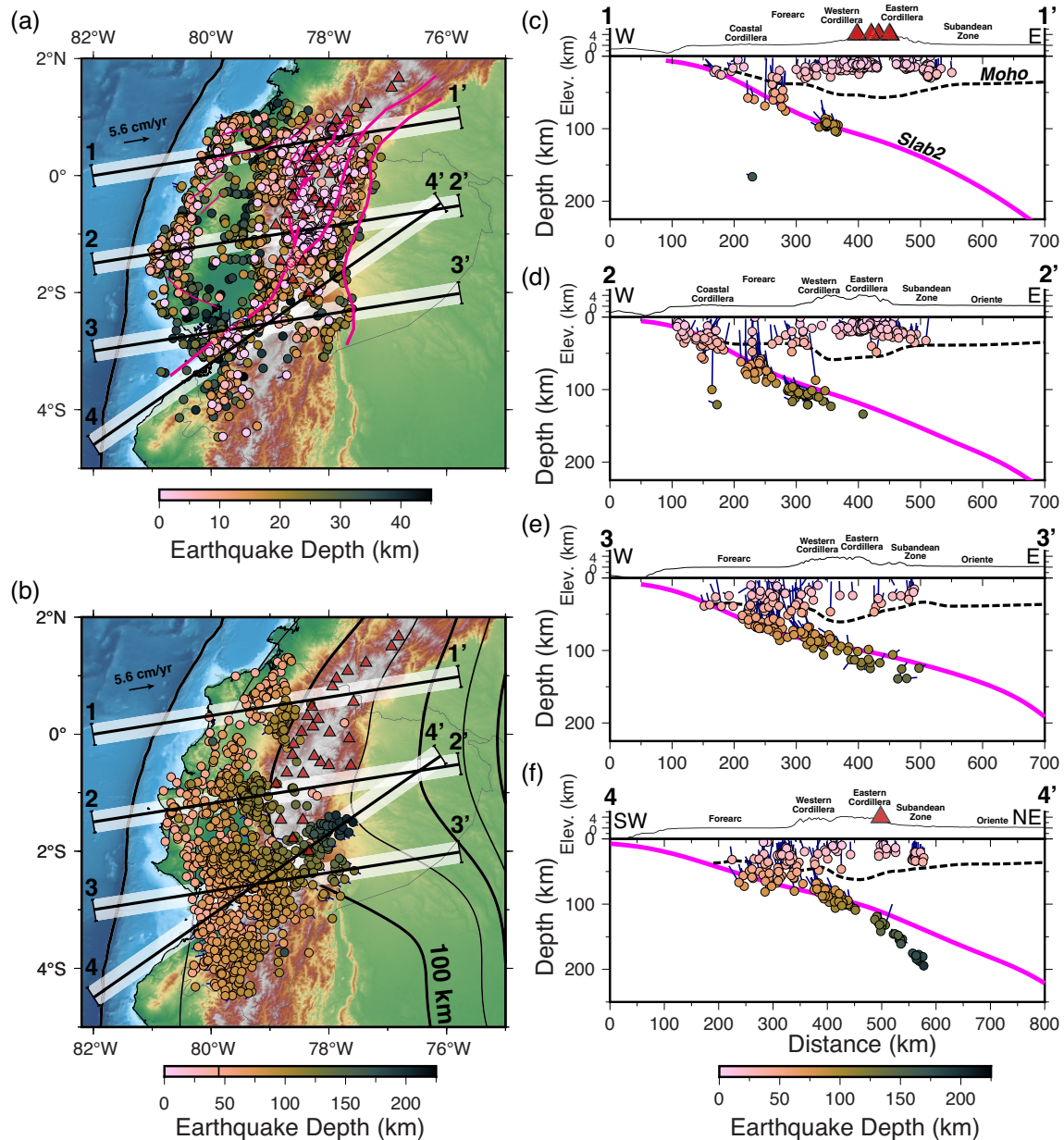
Figure 3. Relocated earthquakes used in this study. (A) Map view of crustal earthquakes and faults (pink lines). Blue lines show the change in hypocentre location from initial to final. We note that earthquake hypocentres did not change very much when relocated. Coloured circled show the final location of the earthquakes re-located in our model (<45 km depth). Major tectonic regions and faults are highlighted. Red triangles—Holocene Volcanos. Major faults are highlighted in pink. (B) Earthquake locations below 45 km depth. Blue lines show the change in hypocentre location from initial to final. Coloured circled show the final location of the earthquakes re-located in our model. Black lines contour the Slab2 model of the Nazca slab at every 50 km depth (Hayes *et al.* 2018). (C–F) Cross-sections 1, 2, 3 and 4 showing the earthquake locations projected within 20 km (shaded area in A and B) and the Slab2 model (Hayes *et al.* 2018) for cross-section lines shown in A and B. The dashed black line shows Koch *et al.* (2020)'s estimates of the continental Moho beneath Ecuador.

data stopped changing significantly (Supplementary Fig. S3). The inversion also includes standard damping and smoothing regularization but also allows for *a posteriori* smoothing of perturbations. For our model, *a posteriori* smoothing is applied at each iteration by a 5 km moving average window both laterally and with depth. The model space extends from 12 km above sea level to 400 km depth and from 83°W, 2°N to 75°W, 6°S and node spacing is defined as 0.05° longitude, 0.05° latitude and 5 km depth (Fig. 4D).

Our starting model is a 3-D velocity hybrid model based on Poveda *et al.* (2015), Koch *et al.* (2021) and IASP91 (Kennett & Engdahl 1991), where we use the 1-D *P*- and *S*-wave velocity model from IASP91 and modify the depth of the Moho to reflect the 3-D crustal thickness model of Koch *et al.* (2021) and Poveda *et al.* (2015; Figs 4 and S4). We additionally choose to remove the sharp discontinuities from the IASP91 velocity model to make the crust more gradational and replace the Moho with a gradation of velocities over a 5 km interval. Further examples of other starting models with their resultant seismic images are shown in Supplementary Figs S5 and S6, including 1-D *P*- and *S*-wave velocity model from IASP91 and a hybrid 3-D Moho model with
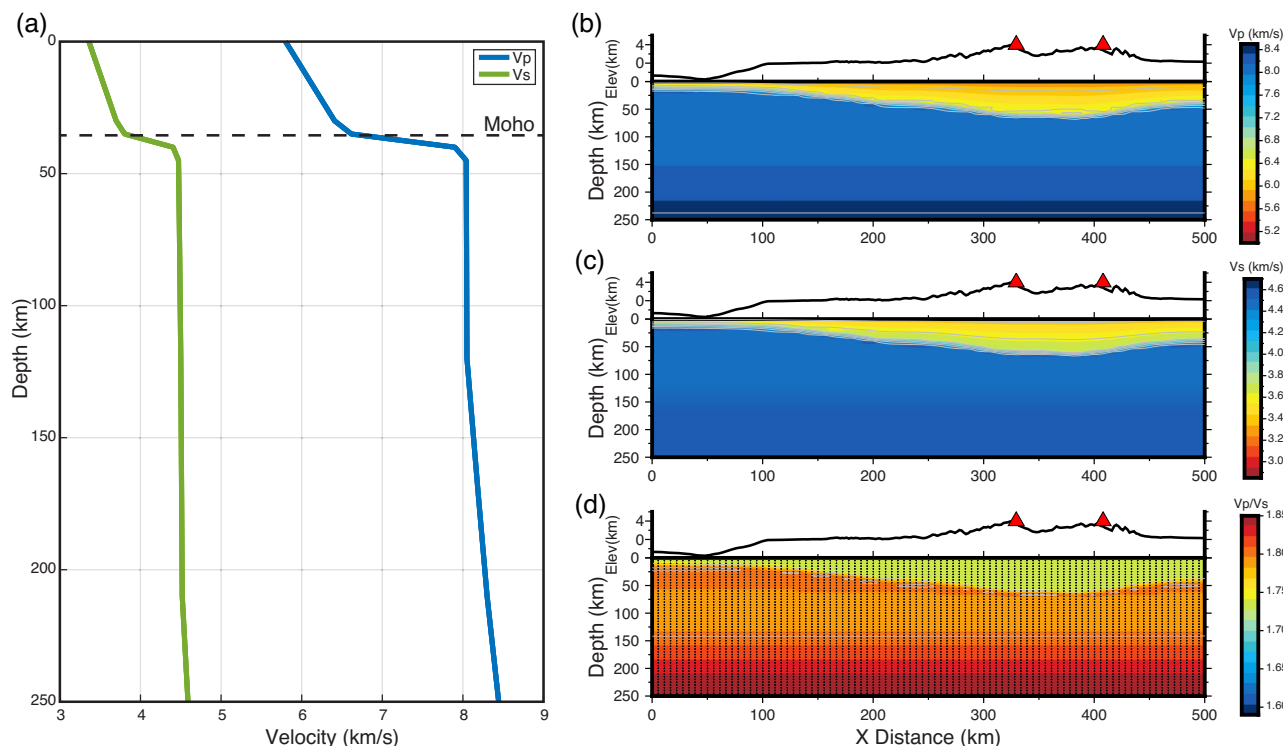
Figure 4. Starting velocity model. (A) The IASP91 1-D velocity model for *P*- (blue) and *S*-wave (red) velocity (Kennett & Engdahl 1991). (B) The 3-D variable Moho starting *P*-wave velocity model. Moho depth estimations are from Koch *et al.* (2021) and Poveda *et al.* (2015; Fig. S1). (C) The 3-D variable Moho starting *S*-wave velocity model. (D) The 3-D variable Moho starting V_p/V_s model. Small black dots represent the model node centre for the model (0.05° latitude by 0.05° longitude by 5 km depth).

IASP91 velocities, including discontinuities. We interpret anomalies which are consistent across all starting models. We note that changes to the starting models resulted in the velocities of anomalies across inversions to be reasonably comparable, however, the depth of these anomalies were strongly controlled by the presence of discontinuities. We therefore chose a starting model with no strong discontinuities to reduce this effect.

3.1 Resolution tests

To assess the resolution of our model, we rely on synthetic anomaly tests. The first of these tests is a synthetic checkerboard model (Figs 5 and 6). For this test we input alternating $\pm$ 5 per cent V_p and $\pm$ 5 V_s as synthetic anomalies into our model every 6 nodes ($\sim$30 km), with 3 nodes ($\sim$15 km) of 0 per cent V_p and V_s in between. We calculate the checkerboard output using our station locations and hypocentres of our final model earthquake locations. The recovered checkerboards reveal that the synthetic input recovery is dependent to first order by the distribution of surface waves and local earthquakes, with very low dependence on ray paths from teleseismic earthquakes. For our model, we have the highest recoverability in the crust, above $\sim$30 km depth beneath the forearc and arc, where we recover > 50 per cent of our synthetic input anomaly. In addition, Supplementary Figs S7 and S8 show ray hit-count cross-sections for the *P* and *S* waves, respectively, for our final model.

Overall, depth resolution in our model is best above the slab in the upper 30 km but increases in depth under the arc. We have resolution down to $\sim$50–80 km beneath the arc but no resolution beneath the slab. Below 30 km, synthetic anomaly recovery (Fig. 6) is limited by

local event-station locations. Earthquakes in this model are limited to 210 km depth, with the majority of events ($\sim$75 per cent) located above 50 km depth (Figs 3 and 6). Between $\sim$1°N and 2°S we have good recovery of the input anomaly amplitude ($\sim$50 per cent of the true value) and shape are well recovered from $\sim$5 to $\sim$80 km depth. We do not recover any input anomalies below where the local earthquakes are located, limiting resolution to above the subducting slab. In a synthetic slab recover test (Supplementary Figs S9–S10), we are unable to recover much of the synthetic slab below 50 km depth.

4 RESULTS

4.1 Relocated Seismicity

The initial and final locations of earthquakes are shown in map view (Fig. 3) and cross-sections (Figs 3, 9 and 10). Seismicity used in our final model is largely located within the upper plate, as the slab seismicity is sparse. Of the earthquakes used within the model, 3693 (more than 70 per cent) occurred at depths above 40 km. Seismicity in the upper plate is largely concentrated in the Coastal Cordillera, active volcanic arc, including the Western and Eastern Cordilleras, and thrust faults of the Subandean Zone. Between the Coastal and Western Cordilleras there is sparse seismicity beneath the Manabí Basin which overlaps with a gap in seismic stations.

Along the westernmost margin of the upper plate, seismicity extends from the base of the crust to the surface across the margin between 1°N and 2°S (e.g. Fig. 3). Seismicity is largely active along thrusts along the Coastal Cordillera and along the plate interface.
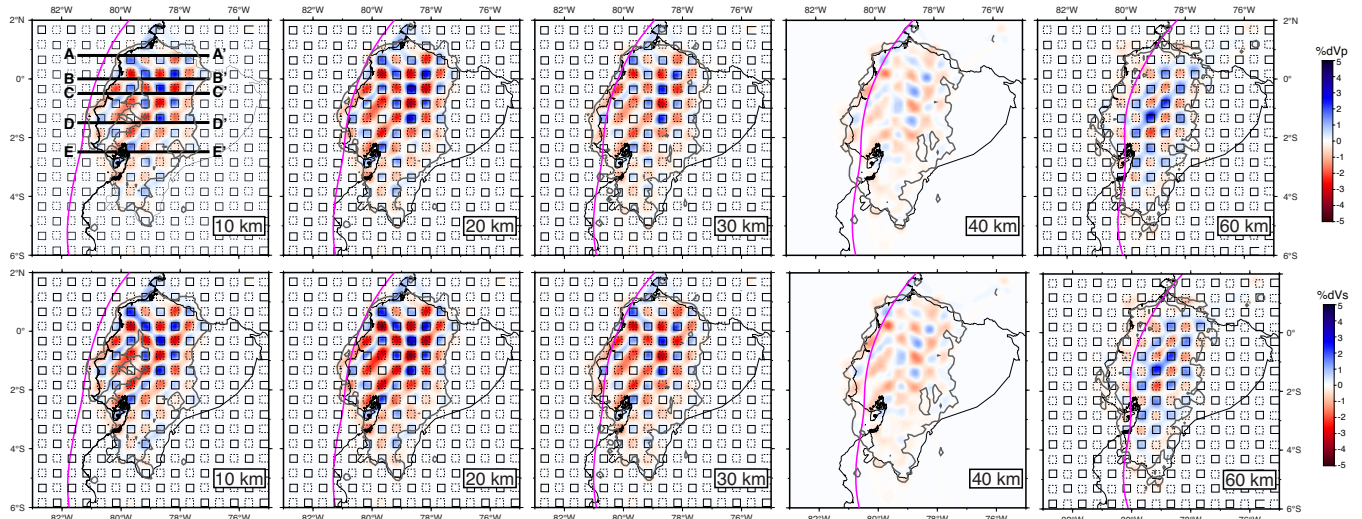
Figure 5. Depth slices through synthetic checkerboard tests. Black squares define the synthetic input anomalies. Dashed lines show input checkers of −5 per cent V_p (top row) and V_s (bottom row). Solid lines show input checkers of +5 per cent V_p and V_s. The dark grey contour line encloses nodes within the model with > 5 sampling rays. We note that the 40 km layer does not have any synthetic anomalies within it.
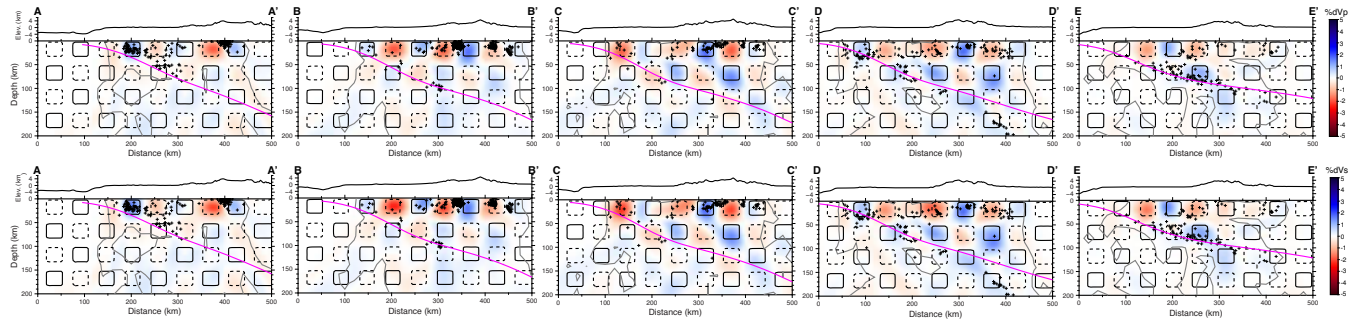

Figure 6. Cross-sections through synthetic checkerboard tests. We refer to Fig. 5 for the location of each cross-section. Black lines define the synthetic input anomalies. Dashed lines show input checkers of −5 per cent V_p (top row) and V_s (bottom row). Solid lines show input checkers of +5 per cent V_p and V_s. The dark grey line contours nodes within the model with > 5 sampling rays.

We note that our data set does include the aftershock sequence of the 2016 M7.8 Pedernales earthquake and the denser station spacing deployed in the forearc in response to the megathrust.

Earthquakes occurring below the arc are on average shallower than the bordering regions of the forearc and Subandean Zone, averaging <10 km depth (e.g. Figs 3C–D). The maximum depth of crustal earthquakes increases away from the volcanic arc, likely reflecting a change in the geotherm. South of the active arc, a similar pattern emerges where depths recorded deepen to an average of ∼20 km and extend to ∼40 km depth along the CCPP Fault Zone (e.g. Fig. 3A).

Earthquakes below 40 km depth are shown in Fig. 3(B). These events largely occur along a single surface and follow the Slab2 model (Hayes *et al.* 2018) of the downgoing Nazca slab in the upper 100 km (e.g. Figs 3D and F). We therefore refer to these events as the intraslab seismicity of the Nazca plate beneath Ecuador. Intraslab seismicity is limited to the upper 210 km with the deepest cluster of events recorded in our catalogue at 78°W and 1.5°S (Figs 3B and D). This cluster, and earthquakes located updip of it, define a slab slightly steeper than the Slab2 model (Hayes *et al.* 2018). North of this cluster, seismicity disappears below ∼120 km depth beneath the volcanic arc. An additional gap in slab seismicity occurs at 79°W

and 0.5°S with no seismicity located between 40 and 100 km depth (Fig. 3B).

4.2 Tomographic models

Our final *P*-wave, *S*-wave and V_p/V_s velocity models are shown in depth slice and cross-section form in Figs 7–11. We include additional cross-sections of the full model in Supplementary Figs S11–S15. Based on the output of our synthetic tests, we focus our results on the crust and largest anomalies within the model (>30 km width) and portions of the model which have > 5 ray sampling paths above the subducting Nazca plate. For the *P*-wave velocity model, resulting velocities in our model range from 4.9 to 9.2 km s^{-1}, and the *S*-wave velocity model has velocities ranging from 2.7 to 4.9 km s^{-1}. For V_p/V_s of the crust, values range from 1.67 to 1.87.

At shallow depths (<20 km), a continuous slow velocity anomaly in both *P*- and *S*-wave models is imaged along the western forearc (western margin of the continent) between 1°N (northern limit of our model) and 3.5°S where the continental shelf begins to widen. The anomaly is slowest beneath the Borbón and Progreso basins, with *P*-wave velocities of 4.9–5.1 km s^{-1} and *S*-wave velocities of 2.9–3.1 km s^{-1}, at ∼10 km depth (anomalies S1 & S2; Figs 7–11).
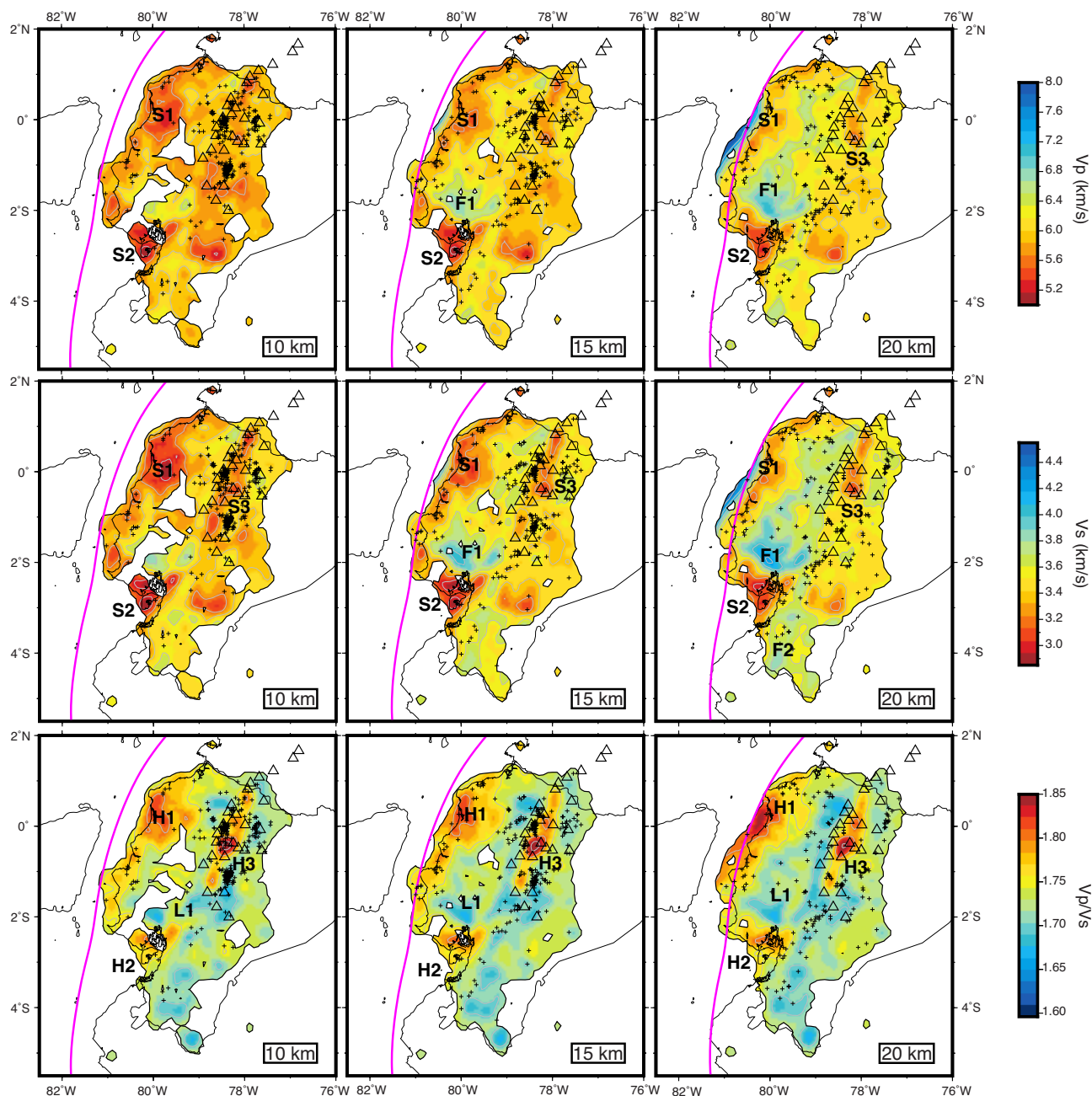
Figure 7. Depth slices through our final V_p (top row), V_s (middle row) and V_p/V_s models (bottom row). Corresponding depths are shown in the lower right corner of each depth slice. Holocene volcanoes are plotted on each depth slice as triangles. Magenta line shows the top of the Nazca slab from Slab2 (Hayes *et al.* 2018). Black crosses show the locations of earthquakes used in the inversion that are located at each depth slice.

These slow velocities are additionally characterized by a relatively high V_p/V_s of 1.82 (H1 & H2; Figs 7–11).

Beneath the central forearc and Western Cordillera from the northern edge of our model to 2.5°S is a region of fast crustal velocities in the lower crust from 18 km depth to the base of the crust (F1; Figs 7–11). This fast lower crust is characterized by P- and S-wave velocities of 6.8–7.2 and 3.8–4.0 km s^{-1}, respectively, and a relatively low V_p/V_s of 1.67–1.70 (L1; Figs 7–10). The connection of this fast material above 20 km is ambiguous due to limited resolution at the centre of the forearc. However, the general surface of the anomaly appears to gently dip northward with the shallowest portion of the anomaly outcropping at the top of our model at the

edge of the Chongón–Colonche Fault, just north of the Progreso Basin (Fig. 7).

Beneath the volcanic arc, slow crustal P- and S-wave velocities as slow as 5.4 and 3 km s^{-1}, respectively, are imaged throughout the crust (anomaly S3; Figs 7–10). These slow crustal velocities trend NNE-SSW, following the axis of the volcanic arc. The centre of the slow velocities occurs just east of the volcanic front and are limited to ~30 km depth in the northern segment of the arc and shallow southward to above 20 km depth at the southern end of the arc (Figs 9–10). A high V_p/V_s anomaly of 1.8–1.87 overlaps with the slow crustal velocities at the centre of the Ecuadorian arc and in some cross-sections extends throughout the crust (H3, Figs 7–11).
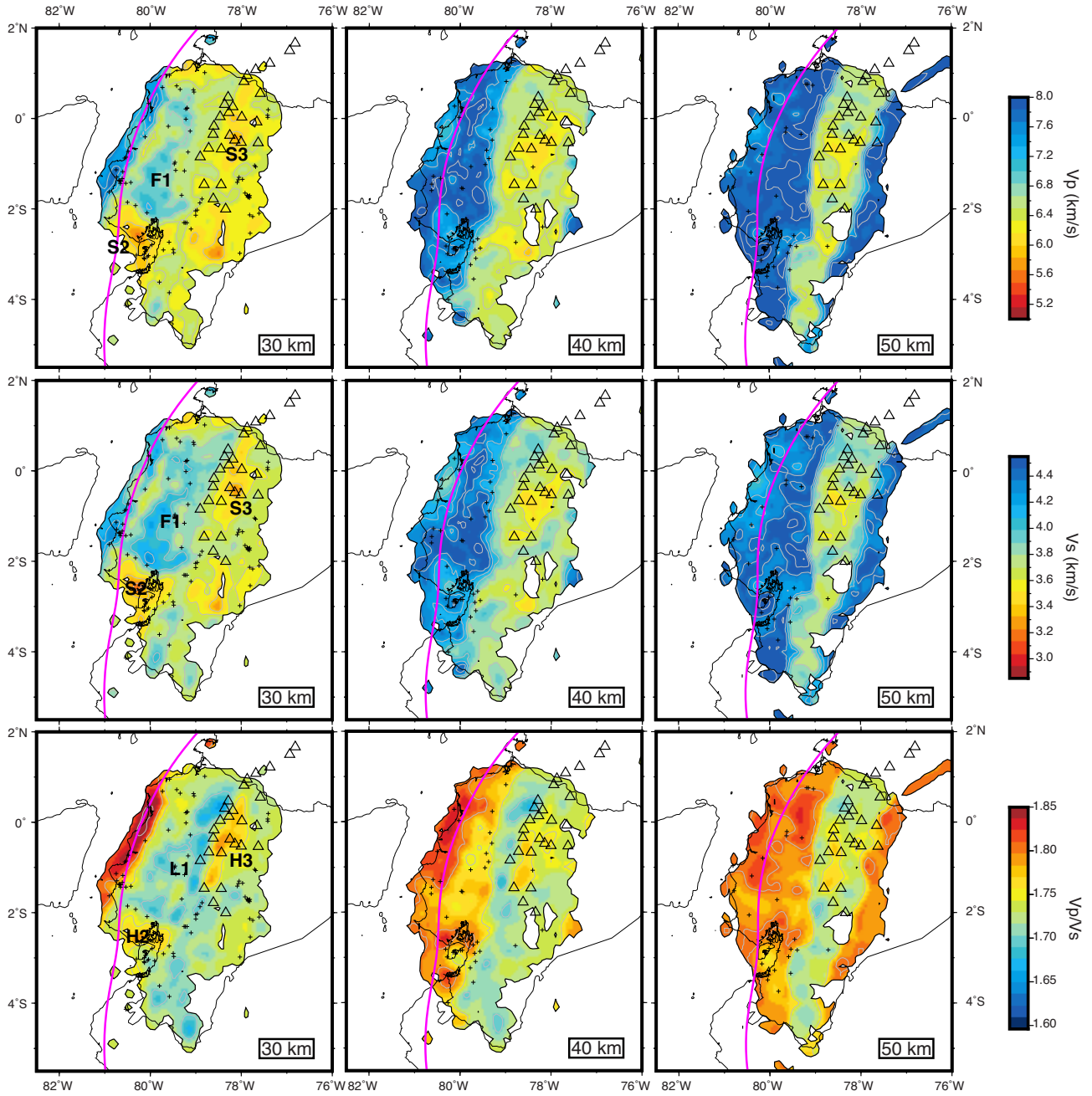
Figure 8. Depth slices through our final V_p (top row), V_s (middle row) and V_p/V_s models (bottom row). Corresponding depths are shown in the lower right corner of each depth slice. Holocene volcanoes are plotted on each depth slice as triangles. Magenta line shows the top of the Nazca slab from Slab2 (Hayes *et al.* 2018). Black crosses show the locations of earthquakes used in the inversion that are located at each depth slice.

We also observe large variations in the seismic velocities and V_p/V_s in the lower crust from west to east (Figs 7–11).

The Nazca slab shows up beneath the forearc at ~30 km depth as a high *P*-wave and *S*-wave velocity and high V_p/V_s. Our image of the Nazca slab is shallower than the Slab2 model in this region (Hayes *et al.* 2018). This may be in part related to our starting model as the forearc crust is thin ~25–30 km deep. But the starting model has a lower V_p/V_s so we suggest that this high V_p/V_s is a signature of the subducting slab.

5 DISCUSSION

Seismic velocities are sensitive to many factors, such as composition, anisotropy, temperature and the presence of fluids. The ratio of *P*- and *S*-wave velocities, V_p/V_s, is also affected by composition, including fluids and partial melt (Christensen 1996). At shallow depths, variations in seismic velocities correlate well with geologic structures. In this section, we discuss our interpretation of our tomography model in the forearc, active magmatic arc, subandean zone and the subduction of the Carnegie Ridge (Table 1).
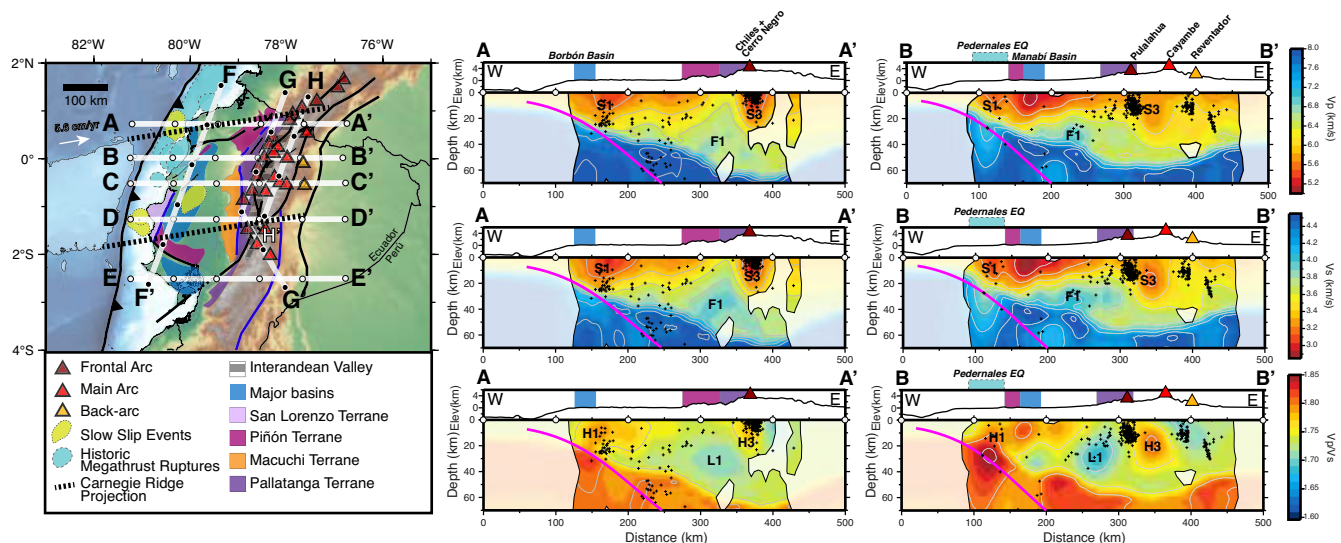
Figure 9. Cross-sections through V_p (top row), V_s (middle row) and V_p/V_s models (bottom row). Left: Generalized geologic map of Ecuador showing the locations of cross-sections. The locations of recorded slow slip events are shown in green (Vallée *et al.* 2013; Rolandone *et al.* 2018; Segovia *et al.* 2018). Major megathrust ruptures areas are plotted in light blue (Kanamori & McNally 1982; Swenson & Beck 1999; Nocquet *et al.* 2017). The light grey dash line shows the potential inboard projection of the Carnegie Ridge following plate convergence direction. We note that there are no present constraints on its projection. Major faults are shown as black lines and suture zones in dark blue lines (we refer to Fig. 1 for names). Right: Cross-sections through V_p (top row), V_s (middle row) and V_p/V_s models (bottom row). Plotted above the topography are major geologic outcrops. Legend corresponds to the figure on the right. Volcanoes within 10 km of the cross-section are shown as triangles and labelled in bold.
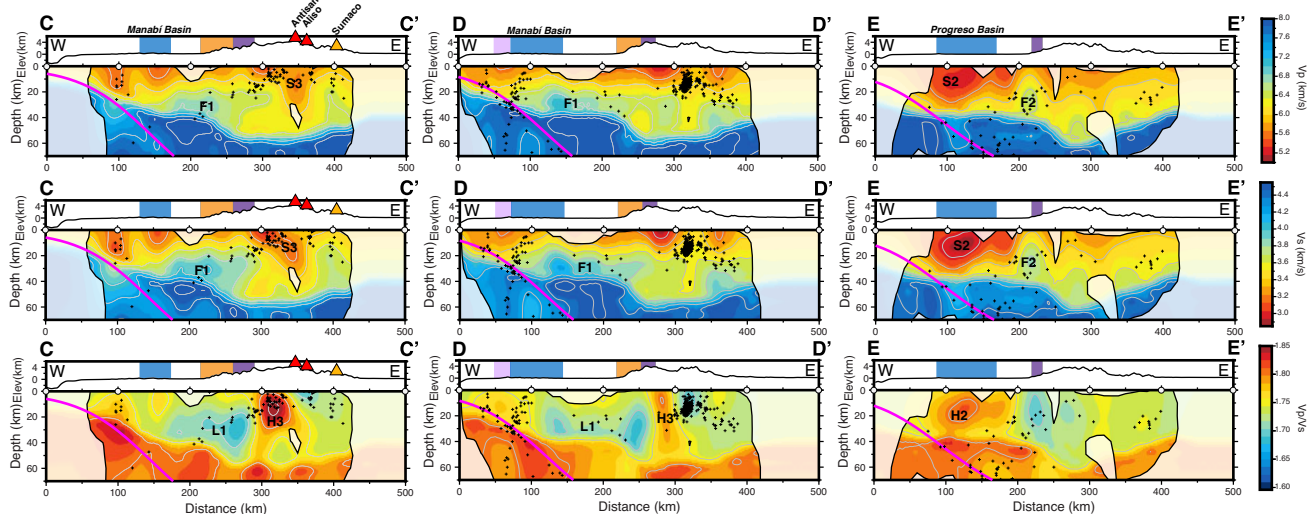

Figure 10. Cross-sections through V_p (top row), V_s (middle row) and V_p/V_s models (bottom row). Each cross-sections includes topography above. Behind the topography is plotted major terranes and basins (see Fig. 9 for legend). Black crosses show the hypocentres of earthquakes from this study. Red triangles show the location of Holocene volcanoes within 10 km of the cross-section. The names of each volcano are shown above in the top row.

5.1 Forearc

The forearc in our tomographic model has predominately high seismic velocities for the average continental crust except for the coastal forearc that has anomalous low seismic velocities and a high V_p/V_s ratio (e.g. Fig. 7). We discuss each of these regions below.

5.1.1 Accreted oceanic terranes

The surface outcrop of Piñón terrane is well-defined in the Ecuadorian forearc and coincides with regions of high seismic velocity (V_p–6.8–7.2 km s^{-1}; V_s–3.8–4.2 km s^{-1}) at ∼10 km depth. At ∼20 km

depth, these regions connect to form the basement of the forearc crust between 1°N and 3°S, extending to the base of the forearc (anomaly F1; Figs 7–10). We attribute this fast velocity material to the mafic Piñón terrane. The high seismic velocities of the Piñón terrane are notably characterized by low V_p/V_s values (∼1.65, anomaly L1; Figs 7–10). The Piñón terrane has been interpreted as an oceanic plateau fragment due to its geochemistry and basalt-dominated composition (e.g. Kerr *et al.* 2002). The *P*-wave velocities of oceanic plateaus range from 6.4 to 7.4 km s^{-1} in the lower crust (e.g. Operto & Charvis 1996; Miura *et al.* 2004; Worthington *et al.* 2012). These velocities are consistent with our images of the Piñón terrane which
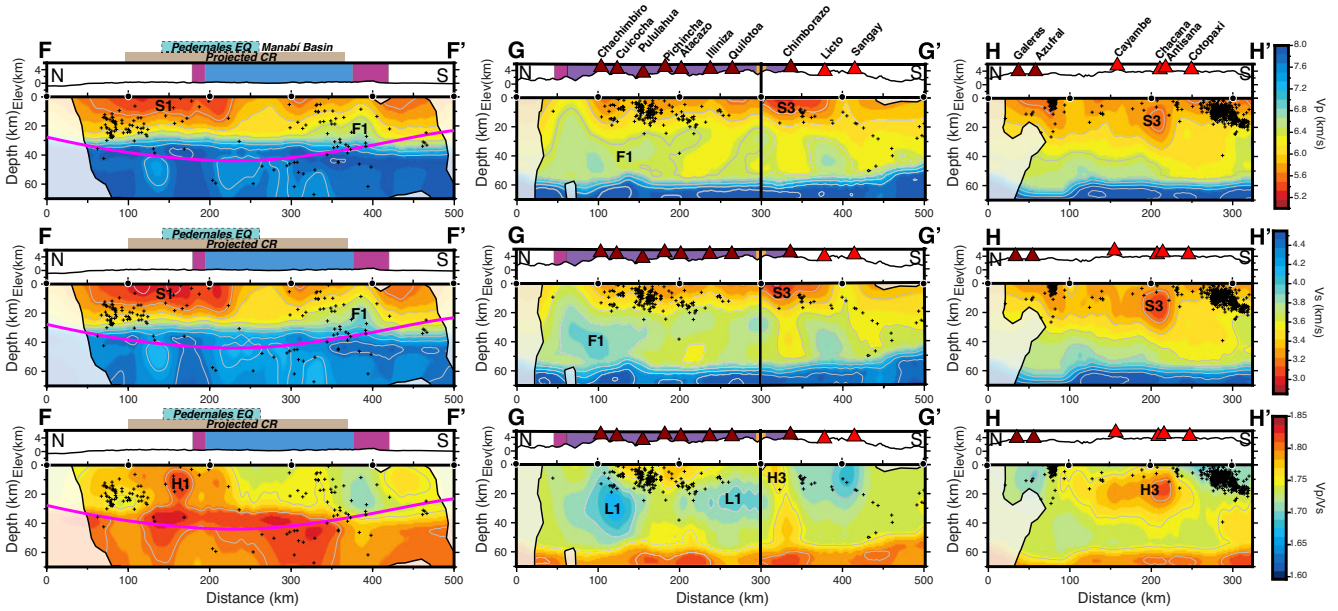
Figure 11. Cross-sections through V_p (top row), V_s (middle row) and V_p/V_s models (bottom row). Each cross-section line is shown in Fig. 9 (parallel or subparallel to trench) and includes topography plotted above. Behind the topography colours indicate major terranes and basins exposed at the surface (see Fig. 9 for legend). Black crosses show the hypocentres of earthquakes from this study. Red triangles show the location of Holocene volcanoes within 10 km of the cross-section. The names of each volcano are shown above in the top row.

Table 1. Seismic anomalies labelled in figures with our interpretation.

V_p and V_s anomaly labels	*Interpretation*
F1	High velocity due to the Piñón/Pallatanga Block in the forearc and Western Cordillera
F2	High velocity due to the Piñón/Pallatanga Block in the forearc and Western Cordillera
S1	Low velocity due to Borbón Basin and hydrated/fractured western forearc
S2	Low velocity due to the Progreso Basin and hydrated/fractured western forearc
S3	Low velocity from partial melt in Volcanic Arc
V_p/V_s anomaly labels	***Interpretation***
H1	High V_p/V_s due to hydrated/fractured forearc
H2	High V_p/V_s due to Progreso Basin
H3	High V_p/V_s due to partial melt in volcanic arc
L1	Low V_p/V_s in Piñón Block in the central forearc

is characterized by velocities of 6.8–7.2 km s^{-1} and with previous studies that have inferred the basement of the Ecuadorian forearc is comprised of oceanic accreted material (e.g. Luzieux *et al.* 2006; Koch *et al.* 2020).

Lynner *et al.* (2020) imaged the same high velocity region beneath the central forearc using ambient noise tomography. In the Lynner *et al.* (2020) model, the coastal and central forearc is similarly characterized by high *S*-wave velocities of 3.7–4.4 km s^{-1} below 20 km depth. They infer these velocities to be of mafic mantle affinity and associate them with the lithospheric mantle of the Piñón/Pallatanga terranes or the Carnegie Ridge (Lynner *et al.* 2020). We include

their data in this study, so it is not surprising that we observe the same high velocities in the central forearc. With the addition of local and teleseismic earthquake traveltimes, the high velocity zone in our model is relatively slower than that of Lynner *et al.* (2020), with velocities of 3.8–4.2 km s^{-1} that are more consistent with oceanic crustal velocities of the crustal component of the Piñón terrane.

The eastern limit of the Piñón terrane at the surface is bounded by the Macuchi and Pallatanga blocks beneath the Western Cordillera. We image no clear distinction between these blocks seismically E–W. The Macuchi block is distinct in its composition of volcaniclastic deposits compared to the Piñón terrane of mafic–ultramafic rocks (e.g. Hughes & Pilatasig 2002). This would imply that the two blocks should be seismically distinct in their velocities, however, the lower crust of the forearc, from the coast to the active arc, does not show significant variation that correlates with this juxtaposition. Isotopic analysis of the volcanic rocks of the Macuchi block suggests the magma was sourced at deep crustal levels and contaminated by basement composed of oceanic plateau material (e.g. Chiaradia *et al.* 2004, 2009; Vallejo *et al.* 2016). The lack of a distinct velocity anomaly associated with the Macuchi block may be attributed to: (1) the basement beneath the block is mafic oceanic plateau material, as suggested by its geochemistry, and therefore not seismically distinct, or (2) the deeper crust of the block was not preserved during or following accretion.

In northern Ecuador, where the Pallatanga block outcrops adjacent to the Piñón terrane in the Western Cordillera, we see a slight decrease in seismic velocity from the edge of the arc east towards the coast in the upper ~30 km (e.g. Fig. 9). Anomaly F1 (Fig. 9, cross-section A) extends towards the surface beneath the Pallatanga block at this latitude (~1.5°N). In cross-sections of our model farther south the F1 anomaly extents westwards under both the Pallatanga and Macuchi blocks (Figs 9 and 10). Hence, at this latitude, we hesitate to correlate it with a particular block. South of the volcanic arc (~2.5°S), a similar crustal high velocity zone is observed beneath surface outcrops of the Pallatanga block (anomaly

F2; Figs 7–11). We infer this anomaly to be related to the Pallatanga block, which is disconnected from the Piñón terrane anomaly (F1) by the CCPP fault zone. In most of the model, both the Pallatanga and Piñón blocks are comparable in seismic velocities ($\sim$6.8–7.2 V_p; $\sim$3.8–4 km s^{-1} V_s) and relatively low V_p/V_s (1.65–1.70).

Work by Vallejo *et al.* (2019) suggests the Pallatanga and Piñón blocks are geochemically equivalent and that the two blocks are a single unit that is connected at depth. In this model, the Macuchi island arc block formed on top of the Pallatanga/Piñón block and then accreted to the continent, rather than prescribing three successive accretionary events for the Pallatanga, Macuchi and Piñón blocks (e.g. Vallejo *et al.* 2019). Although our image cannot discern this relationship, it is consistent with this model.

We observe significant differences in the velocities of the crust across the Eastern and Western Cordilleras and backarc regions of Ecuador (Figs 7–10). From our models, high velocities and low V_p/V_s anomalies (F1, F2 and L1) are limited in their eastward extent to Western Cordillera where a clear delineation is obscured by the volcanic arc that is lower in velocity in our model. We infer that there is a major crustal boundary between the accreted oceanic terranes and the South American continent, presumably beneath or bounded by the arc as previously postulated by Koch *et al.* (2021). We interpret the transition from high-to-low velocities and low-to-high V_p/V_s as the boundary between the more mafic basement under the Western Cordillera and the continental basement under the Interandean Valley and the Eastern Cordillera (Figs 10 and 11). This major terrane boundary has a variable dip from an east dip to a near vertical dip and is visible throughout the upper plate seismic images (Figs 7–10).

5.1.2 Faulting and hydration of the coastal forearc

The western limit of the oceanic terranes is unclear from seismic velocities alone. Along the coastal cordilleras (western forearc), the San Lorenzo and Piñón blocks crop out along the coast, however there are no distinct high velocities associated with either in our models as expected from their mafic compositions. Instead, the upper plate along coast of Ecuador is characterized by low velocities ($<$5.2 km s^{-1} V_p and $<$3 km s^{-1} V_s) and high V_p/V_s ($>$1.8) as far as $\sim$260 km inboard of the trench and to a depth of $\sim$20–25 km (anomalies S1 and H1; Figs 7–11). Lynner *et al.* (2020) and Koch *et al.* (2020) also observed a region of distinctly low shear velocities ($<$3 km s^{-1} V_s) beneath the forearc in the Manabí basin. Previous studies, mainly focused on the aftershock sequence of the 2016 Pedernales earthquake, report similar velocities (5–5.5 km s^{-1} V_p) and high V_p/V_s ($>$1.85) beneath the Manabí basin and around Esmeraldas (Hoskins *et al.* 2021; León-Ríos *et al.* 2021).

The low velocities and high V_p/V_s along the coast of central Ecuador contrast with the velocities reported for the forearc of central Colombia, where oceanic terranes extend northwards (Fig. 1A). In this region, Syracuse *et al.* (2016) observed forearc V_p and V_s velocities of 7 and 3.7 km s^{-1}, respectively, that are higher than what we observe in the Ecuador forearc where the CR is subducting. Similar high seismic velocities have been reported along much of the South American forearc (Perú and Chile), which is primarily composed of older batholithic materials (not oceanic accreted terranes) resulting from subduction erosion along the margin (e.g. Koulakov *et al.* 2006; Schurr *et al.* 2006; Gallego *et al.* 2010; Ward *et al.* 2013; Lynner *et al.* 2018). Hence, these low velocities are likely in part due to a different composition.

Low velocities of the Ecuador coastal forearc and cordillera coincide with the inboard projection of the subducted CR, although to a more limited extent. León-Ríos *et al.* (2021) attribute the low seismic velocities in their model to fracturing and possible hydration in the overriding plate due to the subduction of the thick oceanic crust of the CR. Hydration and fracturing of the coastal forearc explain the lack of high seismic velocities associated with the mafic Piñón and San Lorenzo terranes which outcrop along the coastline. Both faulting and fluids would decrease seismic velocities and are consistent with the observed high V_p/V_s. León-Ríos *et al.* (2021) suggest the heavily fractured and hydrated oceanic crust of the CR, evidenced by seismically active extensional faults within the CR has led to a localized release of fluids into the overriding plate as the ridge subducts. Active seismic trench surveys offshore including the Carnegie Ridge show bathymetry consistent with outer rise normal faults as it enters the trench (Marcaillou *et al.* 2016). Normal faults often provide conduits for water to get into the downgoing oceanic lithosphere that then release fluids as they subduct due to increasing pressure. Chesley *et al.* (2021) suggest that in the Hikurangi trench, east of New Zealand, subduction of seamounts and the Hikurangi plateau with thick oceanic crust (1–11 km) produces a fluid rich damage zone that can modulate fluid release into the upper plate. The CR may play a similar role as it subducts beneath the Ecuador coast.

Additionally, the Coastal Cordillera, which initially uplifted $\sim$5.3 Ma (Collot *et al.* 2019), is actively deforming, as supported by the ongoing seismicity along coastal faults (e.g. this study; Beauval *et al.* 2013; Font *et al.* 2013; Soto-Cordero *et al.* 2020; Hoskins *et al.* 2021; León-Ríos *et al.* 2021). A highly fractured upper plate crust along the coastal forearc may in part explain the relatively low seismic velocities and/or provide additional channels to hydrate the overriding plate.

Evidence in support of a hydrated forearc includes the concurrence of slow-slip seismic events (SSEs) and seismic swarms in this region (Fig. 9; Vallée *et al.* 2013; Rolandone *et al.* 2018; Segovia *et al.* 2018; Hoskins *et al.* 2021). SSEs along the plate interface near la Plata Island, at the southern edge of the CR, occurred in 2010, 2013 and again in 2016 following the Pedernales event (Fig. 9; Vallée *et al.* 2013; Rolandone *et al.* 2018; Segovia *et al.* 2018). A series of SSEs north of the CR (Fig. 9; e.g. Vaca *et al.* 2018) and deeper SSEs inboard of the CR at $\sim$60 km depth both before and after the Pedernales earthquake have also been recorded (e.g. Rolandone *et al.* 2018). Aseismic slip along SSEs has been associated with elevated pore-fluid pressure from hydration (e.g. Liu & Rice 2007). Hoskins *et al.* (2021) analysed seismic swarms near Esmeraldas following the 2016 event and found the swarms consistent with fluid diffusion into the upper plate along several shallow faults. Hydration of the mafic upper plate forearc would likely result in serpentinization in the deepest portions of the forearc which may additionally decrease seismic velocities and explain the higher V_p/V_s ratios in the forearc.

Lastly, it is worth noting that these low velocity and high V_p/V_s anomalies coincide with the rupture area of the 2016 M_w 7.8 Pedernales megathrust earthquake (Anomaly H1, Fig. 11, cross-section F; e.g. Nocquet *et al.* 2017). This earthquake ruptured within the same region of the subduction zone as a 1942 M7.8 earthquake (Swenson & Beck 1999), both of which terminated at the same latitude as a 1906 M_w 8.8 earthquake (Kanamori & McNally 1982). South of these ruptures, ($\sim$0.5°S), extending to at least $\sim$3°S and probably farther south, no large magnitude ($>$7.7 M_w) megathrust events have been historically recorded (e.g. Villegas-Lanza *et al.* 2016). The interplay of subduction zone fluids, the megathrust supercycle

and slow slip events has been investigated in many studies. Focused studies on the plate interface have suggested that variable friction across the megathrust zone along strike is linked to the rupture magnitude and area (e.g. Lay *et al.* 2012; Audet & Schwartz, 2013; Moreno *et al.* 2018). Elevated pore pressure from fluids and tectonic loading at subduction zones can also induce faulting by decreasing the effective normal stress. For Ecuador, the correlation between our interpreted region of high fluids and the megathrust-rupturing segment imply they are connected. We cannot distinguish between hydration and a fracturing of the upper plate along the coastal fore-arc as both processes are likely at play with the subduction of the CR.

5.1.3 Low velocities of the Progreso Basin

The Progreso Basin in southern Ecuador is a transtensional forearc basin (Alemán *et al.* 2021) that correlates with slow crustal velocities and high V_p/V_s values. This basin coincides with the southern origination of the CCPP fault zone and the inboard projection of the Grijalva Fracture Zone along the subducting Nazca slab, which is presently at the trench at ∼3°S (Fig. 1). This fracture zone emplaces oceanic crust of 30 Ma adjacent to 21 Ma across the fracture (Hardy 1991). Beneath the Progreso Basin of southwest Ecuador are relatively low *P*- and *S*-velocity anomalies (anomaly S2 in Figs 7–8 and 10–11). In both models, the anomaly extends from the top of our model down to the base of the accreted terrane crust at ∼40 km depth (Fig. 10, cross-section E). The slowest portion of the anomaly is limited to the upper 20 km and is 5–5.2 and 3–3.2 km s⁻¹ for the *P*- and *S*-wave velocities, respectively. These anomalies correlate in map view and cross-section to a high-V_p/V_s anomaly (1.8–1.82; H2 in Figs 10–11), at its centre at ∼20 km depth beneath the Isla Puna, near the southeastern edge of the Progreso Basin.

In the upper crust the low velocities correlate with the Progreso Basin and the CCPP strike-slip fault and the Grijalva Fracture zone in the downgoing Nazca slab. It is likely that the CCPP fault is a conduit for fluids consistent with our seismic velocities. An offshore study of the subduction zone margin by Calahorrano *et al.* (2008), found elevated pore pressures (8–40 MPa) from the trench, extending 25 km in-board, which they interpret as fluid overpressure within the subduction channel. The deeper portions of the anomaly may reflect some amount of serpentinization at depths between 20 and 40 km above the slab.

5.2 Ecuadorian arc

The modern magmatic arc in Ecuador is relatively young (<1 Ma), with some of the most active Quaternary volcanoes in South America and represents a major hazard for many residents (Bablon *et al.* 2019). The arc is broad, extending across the Western and Eastern Cordilleras and eastward into the Subandean zone along the projection of the subducting Carnegie Ridge in central Ecuador (e.g. Fig. 1). As mentioned previously, the subducting Nazca slab is shallow but not flat, as evidenced by the active arc as well as slab seismicity (e.g. Yepes *et al.* 2016).

From west to east, we resolve several differences in the seismic structure of the Ecuadorian arc. Generally, the frontal part of the arc is characterized by shallow, upper crustal, low velocity and high V_p/V_s regions which overlie the fast oceanic terrane material of the Piñón/Pallatanga terrane (Figs 9 and 10). We interpret low velocities and high V_p/V_s zones in arc settings as partial melt of crust. The main arc, beneath the Interandean and Western Cordilleras, is

characterized by low velocities and high V_p/V_s anomalies extending throughout the mid-crust. The most distinct region of partial melt lies in the centre of the main arc, where it broadens eastward into the Subandean Zone. In contrast, the backarc volcanoes, Reventador and Sumaco, show no distinct anomalies directly beneath them in the mid- and lower crust.

5.2.1 The frontal arc

The frontal volcanic arc resides in the Western Cordillera and loosely parallels the trench at ∼250–275 km inboard. Low crustal velocities are limited to the upper crust and contrast with the basement which is composed of the fast velocity material of the Piñón and Pallatanga terranes as described in Section 5.1. Beneath this line of volcanoes, we image seismic velocities of 5.4–5.6 km s⁻¹ V_p and 3.1–3.4 km s⁻¹ V_s in the upper 20 km at the slowest regions of the crust (Figs 7–10 and 11, cross-section G).

The lowest velocities (<5.2 km s⁻¹ V_p and <3.0 km s⁻¹ V_s) beneath the frontal volcanic arc are beneath the Chiles and Cerro Negro volcanic complex in the upper 10 km (Figs 7–8, 9A, and 12H). At the centre of these low velocities, V_p/V_s is 1.78–1.8, which is consistent with an increase in pore-fluid. Koch *et al.* (2021), similarly imaged a zone of low crustal velocities (<2.8 km s⁻¹ V_s) at 10 km depth directly beneath the Chiles and Cerro Negro volcanic complex which they interpret as partial melt in the upper crust. Relocated earthquakes in our model cluster around this slow velocity anomaly and extend from 0 to 20 km depth. Captured in an overlapping earthquake catalogue as used in this study, IG-EPN (2019), reported a seismic swarm between September 2018 and July 2019, recording >147 000 events (<M 3.6; IG-EPN 2019). Seismicity related to this swarm was limited to the upper 20 km depth and interpreted as the upward migration of magma (IG-EPN 2019). Our model lends further support to the Koch *et al.* (2021) and IG-EPN (2019)'s interpretation of partial melt beneath the Chiles-Cerro Negro complex within the upper 10 km of the crust.

From our model, the basement of the frontal arc is composed of the high velocity material (∼6.8–7.2 V_p; ∼3.8–4 km s⁻¹ V_s) of the Piñón and Pallatanga terranes which are of oceanic affinity (anomalies F1 and F2; Figs 7–11). This mafic material, from its seismic velocities, appears largely unaltered by the arc and may act as a structural control which limit the depth of crustal assimilation. Geochemical analysis of lavas across the arc report that crustal contamination is higher in the Eastern Cordillera than in the frontal arc (<10 per cent; Hidalgo et al 2012; Ancellin *et al.* 2017). This model reflects our observations of the arc, which show signs of partial melt limited to the upper 20 km beneath the frontal arc. We note, however, that the MORB-like basaltic basement of the frontal arc makes it difficult to interpret isotopic signatures as derived from the mantle versus crust (e.g. Hidalgo *et al.* 2012).

5.2.2 The main arc

The crust beneath the main arc of the Interandean and Eastern Cordillera is characterized by relatively low velocities (5.6–6.4 km s⁻¹ V_p and 3–3.6 km s⁻¹ V_s) compared to the Western Cordillera. Main arc lavas are more felsic to intermediate in composition compared to the frontal arc, with no signature of the Pallatanga/Piñón terranes from geochemical analysis (Samaniego *et al.* 2010; Ancellin *et al.* 2017). This decrease in velocity maybe representative of a combination of a compositional change in the rocks and potential partial melt beneath the arc. Beneath the central
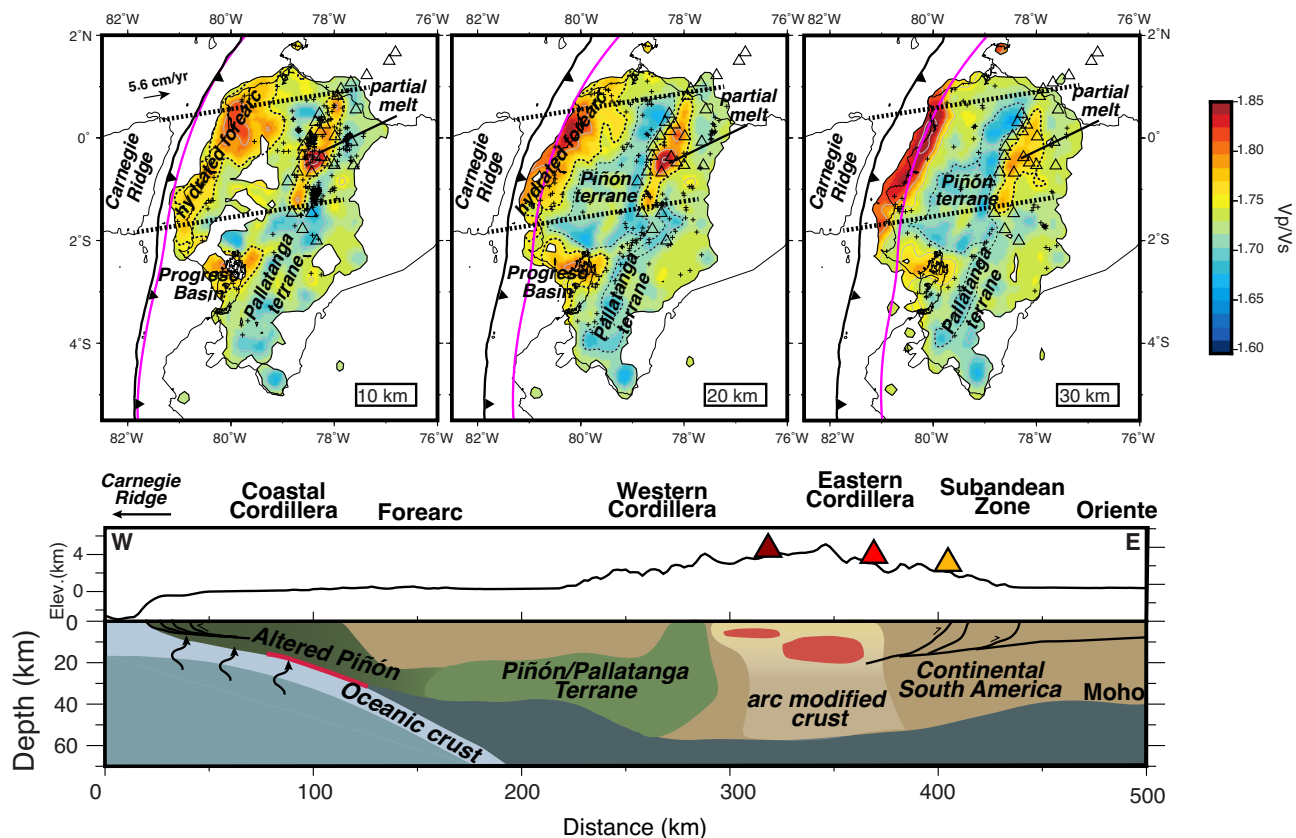
Figure 12. Top: Map view of V_p/V_s from our final tomography model for select depths showing our interpretation with the outline. The projection of the Carnegie Ridge from modern South America/Nazca plate convergence direction is shown as the thick dashed line. Bottom: Schematic illustration of the Ecuadorian Andes across the forearc and arc based on our seismic model interpretation of cross-section B. Volcanoes at the surface shown in triangles colour coded for Western Cordillera, Eastern Cordillera and Subandean zone from west to east, respectively. Rupture from the 2016 Pedernales earthquake (Nocquet *et al.* 2017) plotted as a red line between the plates.

part of the main arc at ∼0.5°S we image a distinct low velocity anomaly (anomaly S3; Figs 8–11). This low velocity zone extends along-strike of the cordilleras and is characterized by a high V_p/V_s (H3) anomaly beneath much of the arc spanning 10–30 km depth (Figs 7–12). The central part of this anomaly lies beneath volcanoes Antisana, Chacana and Cotopaxi (Figs 9–11). These low velocities and high V_p/V_s ratios (∼1.78–1.82) are consistent with partial melt of the crust. Both Antisana and Cotopaxi are considered active and have erupted in the last 200 yr (e.g. Siebert *et al.* 2011). Beneath Cotopaxi, estimates of magma storage depth have ranged between 3 and 17 km depth (Martel *et al.* 2018; Saalfield *et al.* 2019) which is consistent with the depth estimate from our model.

Following Koch's *et al.* (2021) curves of V_s versus percentage of partial melt for main arc in the Eastern Cordillera, we estimate the maximum percentage of partial melt for the S3 anomaly. It is not straightforward to calculate partial melt from V_s velocities due to uncertainties in composition, interconnection of pore-space and a nonlinear relationship between melt, composition and V_s. However, we can make some simple estimates if we assume a composition and then use the V_s and V_p/V_s. Koch *et al.* (2021) assumed the main arc beneath the Eastern Cordillera had a felsic to intermediate composition basement with 62–64 per cent SiO₂ (Samaniego *et al.* 2010; Ancellin *et al.* 2017) based on the recent eruption material there is little direct information about the Eastern Cordillera basement.

Using the lowest V_s, ∼3.1 km s⁻¹, at 20 km depth at the centre of the S3 anomaly, we estimate a maximum of 6.5–9 per cent partial melt (Fig. S16).

Compared to the frontal arc, we image a wider depth range of partial melt regions. The frontal arc has regions of partial melt limited to the upper crust, whereas the main arc displays partial melt throughout the mid-crust. 1-D velocity profiles averaged beneath volcanoes display this general trend (Supplementary Fig. S17). This east–west trend to deeper and larger magmatic reservoirs is also recorded by the geochemistry of arc lavas. Work from Hidalgo *et al.* (2012) and Ancellin *et al.* (2017) show that the volcanic arc lavas increase in crustal assimilation west to east, where it is highest within the main arc. This is true for both upper and lower crust assimilation (Ancellin *et al.* 2017).

5.2.3 The backarc

In contrast to the frontal and main arc, seismic velocities in the backarc are consistent with average continental crust and show no distance regions which would be interpreted as partial melt. These volcanoes are some of the youngest in the arc at <600 ka (Bablon et al., 2019). They are also isolated spatially and lie along the edge of resolution within our model. Given the young age of the volcanoes, it's possible the volcanic arc is not well-developed here, so we might not expect a magma storage body at the same scale as the frontal

and main arc. We additionally note that from our resolution tests, we would not be able to image a low velocity anomaly in this region <30 km wide (e.g. Fig. 4).

The basement of the Subandean zone and backarc is made up of typical continental crustal material. Velocities here are lower than the Piñón/Pallatanga terranes, averaging ∼6 km s^{-1} V_p and 3.5 km s^{-1} V_s, and unlike the Piñón/Pallatanga terranes, V_p/V_s in the backarc (∼1.73–1.75) is more typical of continental crust (e.g. Christensen 1996). We interpret the crust here to be that of continental South America, with the boundary between the accreted terranes and the continental crust somewhere beneath the volcanic arc and likely beneath the Interandean Valley. The basement of the backarc is Precambrian in age and composed of granulites which are overlain by Devonian sedimentary sequences (Feininger 1987).

5.3 A nascent flat slab beneath Ecuador

The relatively young age of the Nazca plate (24–12 My; e.g. Müller *et al.* 2008) and thickness of the CR (15–19 km; Graindorge *et al.* 2004) suggests there should be enough buoyancy force locally to flatten the Nazca slab beneath Ecuador (e.g. Huangfu *et al.* 2016). However, there is little-to-no evidence supporting a significant change in the dip of the downgoing Nazca plate in-board of the ridge. Prior seismic imaging and earthquake re-location work in Ecuador has shown that the slab in-board of the ridge is subducting at a relatively normal angle (∼20°–30°; e.g. Guillier *et al.* 2001; Yepes *et al.* 2016; Araujo *et al.* 2021; Rodríguez *et al.* 2024). The active volcanic arc of Ecuador also indicates that the mantle wedge is still present. Furthermore, the timing of the subduction of the CR is not readily linked to any single event in the overriding plate, which has led to a large range of uncertainty (∼15–1.5 Ma) as to when the CR began to subduct (e.g. Gutscher *et al.* 1999; Longsdale 2005; Michaud *et al.* 2009; Spikings *et al.* 2010). The lack of evidence supporting flat slab subduction and the mystery surrounding the timing of the CR subduction has led many to question how far into the subduction zone the ridge currently is and what it may reveal about the flat slab subduction process.

Considering that similar factors (e.g. oceanic crustal age and thickness) are considered sufficient to induce slab flattening elsewhere in South America (e.g. Peruvian flat slab, Pampean flat slab) when given enough time, we consider it most likely that the CR has not subducted very far into the subduction system and the system is in an early stage of flat slab subduction. We note that for the Pampean flat slab in Chile and Argentina, one of the best studied flat slabs, the Nazca slab took ∼5–6 My to flatten (e.g. Kay & Mpodozis 2002). Based on the magmatic record, it is inferred that the onset of flat-slab formation at current latitudes of 29°–30° began at ca. 11 Ma (Yáñez *et al.* 2001) and reached its current geometry by ca. 5 Ma with the cessation of volcanism ∼5–2 Ma (e.g. Gutscher *et al.* 2000; Kay & Mpodozis 2002; Löbens *et al.* 2011).

Estimates of the CRs arrival in the trench come from a variety of potential markers, including changes in the magmatic arc (both geochemically and spatially; e.g. Samaniego et al., 2005), pulses of uplift across the cordilleras (e.g. Spikings & Crowhurst 2004; Spikings *et al.* 2010; Margirier *et al.* 2023; George et al., 2021), and the re-activation of several fault-systems (e.g. Alvarado *et al.* 2016). Work from Margirier *et al.* (2023) has suggested that earliest estimates of the timing of the CR between 15 and 7 Ma (e.g. Spikings *et al.* 2010), largely recorded in the Eastern Cordillera, represent an earlier stage of cooling and exhumation, unrelated to the subduction of the CR. In their geochronological and thermochronological study,

Margirier *et al.* (2023) see no evidence of this earlier event recorded in the Western Cordillera and instead constrain a distinct uplift event which initiated at ∼6–5 Ma which they attribute to the arrival of the CR at the trench.

Our images of the crust provide some evidence that we may be seeing the beginnings of the slab flattening process and give estimates to timing of the CRs arrival. If the low velocities of the coastal forearc are related to the subduction of the CR, that would emplace it ∼260 km inboard of the trench and ∼180 km from the coast. If this is the extent of the subduction of the CR, then a 5.6 cm yr^{-1} Nazca-South America convergence rate (Trenkamp *et al.* 2002) suggests the ridge has only been subducting ∼4.6 Myr. Volcanoes of the Subandean Zone are the youngest of the arc and our images show no signs of a well-developed magma storage system as we image in the frontal and main arcs to the west. This suggests that the arc is in the process of broadening east. Flat slab subduction is marked by the in-board migration of the volcanic arc as the mantle wedge closes during the flattening process for both the Peruvian and Pampean flat slabs (e.g. Ramos & Folguera 2009). Thus, it is likely that the inboard migration of the volcanic arc is due to the on-going flattening of the Nazca slab from the subduction of the CR. We therefore infer that the buoyant CR has not subducted far enough beneath the system to cause a completely flat slab, but rather we are seeing the process of slab flattening as the arc migrates inboard.

6 CONCLUSIONS

We present *P*, *S* wave and V_p/V_s models across the Ecuadorian forearc, volcanic arc and edge of the Subandean crust from a joint inversion of seismic traveltimes from body and surface waves dispersion. We observe several seismically distinct regions which correlate well with surface geology. Along the coast, low seismic velocities and high V_p/V_s values in the overlying plate (western forearc) coincide with the projection of the Carnegie Ridge beneath the subduction zone. These slow velocities are likely related to a localized increase in fluids released as the ridge subducts and are the consequence of the subduction of the thick oceanic crust which is heavily fractured and hydrated. Active faulting within the Coastal Cordilleras may also facilitate the hydration of the forearc crust. Beneath the central forearc, we image the Piñón/Pallatanga terranes as a high velocity region which comprises most of the lower crust (>20 km depth). The eastern limit of these terranes is obscured by low velocities related to the volcanic arc, however they extend through at least the Western Cordillera.

Our seismic images of the magmatic arc are consistent with a mush zone of partial melt in the lower crust and an upper- to mid-crust anomaly also consistent with some partial melt and indicates that there are multiple storage/stagnation zones within the crust as observed in many other arcs (Delph *et al.* 2017, 2021). The depth of storage varies across the arc and may be limited to the upper crust in the frontal arc, where the arc overlies the oceanic terranes. Beneath the main arc, magmatic storage is at mid-crustal levels and low velocity extends throughout the crust, which may be indicative of a more developed magmatic system with up to 6.5–9 per cent partial melt. Backarc volcanoes in the Subandean zone overlie the continental South American crust and does not show any modification or partial melt in the crust at the scale of our imaging. This suggests we may be seeing the very initial stage of flat subduction from the thick oceanic crust of the Carnegie Ridge. This implies the Carnegie Ridge has not subducted far enough beneath the cordillera system to cause a flat slab geometry.

ACKNOWLEDGMENTS

SUPPORTING INFORMATION

Supplementary data are available at *GJIRAS* online.

Figure S1. Histograms of our initial (left column) and final (right column) model data sets. A–B: histograms for of the initial (A) and final (B) local *P*-wave residual arrival time. C–D: histograms for of the initial (C) and final (D) local *S*-wave residual arrival time. E–F: histograms for of the initial (E) and final (F) teleseismic *P*-wave residual arrival time. G–H: histograms for of the initial (G) and final (H) teleseismic *S*-wave residual arrival time.

Figure S2. Depth slices of tomographic models derived from each data set. Left column—*S*-wave tomography model from surface waves only. The black line delimits the outer edge of interstation paths. Right columns—*S*- (centre) and *P*-wave (far right) tomographic models derived from local and teleseismic earthquakes. The black line delimits model nodes with ≥5 rays. For all depth slices, depth is denoted in the bottom right of the figure. The magenta line indicates the top of the Nazca plate from the Slab2 model (Hayes et al., 2018). Models were created using the same data criteria and model parametrization as described in the main text.

Figure S3. Plot of data RMS versus inversion iteration for teleseismic and local earthquake data. Our final tomography model is shown by the yellow star (iteration 12).

Figure S4. Depth to Moho map of Ecuador used for the starting model. Interpolated model of the depth to Moho derived from Koch et al. (2021) and Poveda et al. (2015). The Carnegie Ridge is outlined in white. Black triangles denote the location of Holocene Volcanoes. The location of the trench is shown as a thick black line.

Figure S5. Effects of different starting models in cross-section. Column 1–The 3-D Moho and IASP91 hybrid model. Column 2–IASP91. Column 3–Same as Column 1 except there are no crustal discontinuities (the velocity model of the crust is a smooth gradient). Cross-section locations are shown on the left. For each cross-section Holocene volcanoes are plotted as red triangles. Earthquake locations from the joint inversion are plotted as crosses.

Figure S6. Map slices of seismic tomography with different starting models. Columns are labelled by the starting velocity model used for the inversion. 3-D Moho IASP91 refers to the IASP91 starting model with the Moho modified (discontinuities are included). 1-D IASP91 refers to the original IASP91 1-D model of Kennett and Engdahl (1991). Left: *P*-wave model. Right: *S*-wave model. For each depth slice, triangles denote the location of Holocene volcanoes.

Figure S7. Ray hit-count cross-sections for the *P*-waves of our final model. Plotted as small crosses are the locations of earthquakes used in the model. The black contour indicates nodes with > 5 ray paths.

Figure S8. Ray hit-count cross-sections for the *S*-waves derived from body waves of our final model. Plotted as small crosses are the locations of earthquakes used in the model. The black contour indicates nodes with > 5 ray paths.

Figure S9. Cross-sections through synthetic slab tests (per cent dV_p). Black lines define the synthetic input anomalies. Solid black lines show input slab of +5 per cent V_p. Black crosses show the locations of earthquakes used in the inversion that are located within 10 km of the cross-section. Each cross-section line is shown in mapview in the upper right corner and includes topography plotted above. Red triangles show the location of Holocene volcanoes within 10 km of the cross-section. Magenta line shows the Slab2 model (Hayes et al., 2018). In general the slab is not well resolved in our synthetic test.

Figure S10. Cross-sections through synthetic slab tests (per cent dV_s). Black lines define the synthetic input anomalies. Solid black lines show input slab of +5 per cent V_s. Black crosses show the locations of earthquakes used in the inversion that are located within 10 km of the cross-section. Each cross-section line is shown in mapview in the upper right corner and includes topography plotted above. Red triangles show the location of Holocene volcanoes within 10 km of the cross-section. Magenta line shows the Slab2 model (Hayes et al., 2018).

Figure S11. Additional *P*-wave velocity cross-sections through the crust of our final model. The scale is in km s^{-1}. Each cross-section line is shown in mapview in the upper right corner and includes topography plotted above. Black crosses show the hypocentres of earthquakes from this study. Red triangles show the location of Holocene volcanoes within 10 km of the cross-section. Magenta line shows the Slab2 model (Hayes et al., 2018). Faint black line is the > 5 ray paths contour. Thick black line shows the depth of the Moho from Koch et al. (2021) which we use as our starting model.

Figure S12. Additional *P*-wave velocity cross-sections through the upper mantle of our final model. The scale is in km s^{-1}. Each cross-section line is shown in mapview in the upper right corner and includes topography plotted above. Black crosses show the hypocentres of earthquakes from this study. Red triangles show the location of Holocene volcanoes within 10 km of the cross-section. Magenta line shows the Slab2 model (Hayes et al., 2018). Faint black line is the > 5 ray paths contour. Thick black line shows the depth of the Moho from Koch et al. (2021) which we use as our starting model.

Figure S13. Additional *S*-wave velocity cross-sections through the crust of our final model. The scale is in km s^{-1}. Each cross-section line is shown in mapview in the upper right corner and includes topography plotted above. Black crosses show the hypocentres of earthquakes from this study. Red triangles show the location of Holocene volcanoes within 10 km of the cross-section. Magenta line shows the Slab2 model (Hayes et al., 2018). Faint black line is the > 5 ray paths contour. Thick black line shows the depth of the Moho from Koch et al. (2021) which we use as our starting model.

Figure S14. Additional *S*-wave velocity cross-sections through the upper mantle of our final model. The scale is in km s^{-1}. Each cross-section line is shown in mapview in the upper right corner and includes topography plotted above. Black crosses show the hypocentres of earthquakes from this study. Red triangles show the location of Holocene volcanoes within 10 km of the cross-section. Magenta line shows the Slab2 model (Hayes et al., 2018). Faint black line is the > 5 ray paths contour. Thick black line shows the depth of the Moho from Koch et al. (2021) which we use as our starting model.

Figure S15. Additional V_p/V_s cross-sections through the crust of our final model. Each cross-section line is shown in mapview in the upper right corner and includes topography plotted above. Black

crosses show the hypocentres of earthquakes from this study. Red triangles show the location of Holocene volcanoes within 10 km of the cross-section. Magenta line shows the Slab2 model (Hayes et al., 2018). Faint black line is the > 5 ray paths contour. Thick black line shows the depth of the Moho from Koch et al. (2021) which we use as our starting model.

Figure S16. Curve showing V_s verses per cent partial melt main arc in the Eastern Cordillera magmatic arcs in the mid-crust from anomaly S3. Diamonds plotted show the intersection of $V_s = 3.1$ km s^{-1} with the curves without (solid green) and with 10 per cent anisotropy (dashed line). Modified from Koch et al. (2021).

Figure S17. 1-D averaged V_p, V_s and V_p/V_s models through the volcanic arc. A) Map view of volcanoes (triangles). Each volcano is coloured by its categorization (see legend within). Circles show the points within the model sampled to create 1-D averaged V_p, V_s and V_p/V_s profiles. Volcanoes are labelled by number: 1–Azufral; 2–Cumbal; 3–Chiles-Cerro Negro; 4–Chachimbiro; 5–Cuicocha; 6–Pululahua; 7- Pichincha; 8–Atacazo; 9–Illiniza; 10–Quilotoa; 11–Chimborazo; 12–Imbabura; 13–Mojanda; 14–Licto; 15–Soche; 16–Cayambe; 17–Chacana; 18–Antisana; 19–Aliso; 20–Cotopaxi; 21–Tungurahua; 22–Sangay; 23–Reventador; 24–Sangay . B.) Averaged 1-D P-wave velocity models through each of the volcanoes (see A). Solid lines show the average, shaded areas show one standard deviation. C) Averaged 1-D S-wave velocity models through each of the volcanoes (see A). Solid lines show the average, shaded areas show one standard deviation. D) Averaged 1-D V_p/V_s models through each of the volcanoes (see A). Solid lines show the average, shaded areas show one standard deviation.

Please note: Oxford University Press is not responsible for the content or functionality of any supporting materials supplied by the authors. Any queries (other than missing material) should be directed to the corresponding author for the paper.

DATA AVAILABILITY

The data are from the Ecuador National Seismic Network (REN-SIG; Ruiz 2016; Alvarado *et al.* 2018), Red Sismológica Nacional de Colombia (Servicio Geológico Colombiano 1993) with open stations provided at the EarthScope Data Center. The initial local earthquake catalogue can be found at RENSIG (https://www.igepn.edu.ec). Data from the temporary station deployments following the 2016 Pedernales earthquake are available at the Earthscope Data Center. The final models and traveltime data will be made available at https://github.com/mlerdrgz/Published-Velocity-models.

REFERENCES

Agurto-Detzel, H. *et al.* 2019. Ridge subduction and afterslip control aftershock distribution of the 2016 M_w 7.8 Ecuador earthquake, *Earth planet. Sci. Lett.,* **520,** 63–76.

Aizprua, C., Witt, C., Brönner, M., Johansen, S.E., Barba, D., Hernandez, M.J. & Billi, A., 2020. Forearc crustal structure of Ecuador revealed by gravity and aeromagnetic anomalies and their geodynamic implications, *Lithosphere,* **2020**(1), 2810692, doi: 10.2113/2020/2810692.

Alemán, A.M., Palencia, A.A., Lezama, E.E. & Montenegro, G., 2021. The Chongón/Colonche orocline transrotational bending and the coeval opening of the Progreso basin in southwestern Ecuador, *J. South Am. Earth Sci.,* **111,** 103480, doi: 10.1016/j.jsames.2021.103480.

Alvarado, A. *et al.* 2016. Partitioning of oblique convergence in the Northern Andes subduction zone: migration history and the present-day boundary of the North Andean Sliver in Ecuador, *Tectonics,* **35**(5), 1048–1065.

Alvarado, A. *et al.* 2018. Seismic, volcanic, and geodetic networks in Ecuador: building capacity for monitoring and research, *Seismol. Res. Lett.,* **89**(2A), 432–439.

Ancellin, M.A., Samaniego, P., Vlastélic, I., Nauret, F., Gannoun, A. & Hidalgo, S., 2017. Across-arc versus along-arc S r-Nd-Pb isotope variations in the Ecuadorian volcanic arc, *Geochem. Geophys. Geosyst.,* **18**(3), 1163–1188.

Araujo, S., Valette, B., Potin, B. & Ruiz, M., 2021. A preliminary seismic travel time tomography beneath Ecuador from data of the national network, *J. South Am. Earth Sci.,* **111,** 103486, doi: 10.1016/j.jsames.2021.103486.

Audet, P. & Schwartz, S.Y., 2013. Hydrologic control of forearc strength and seismicity in the Costa Rican subduction zone, *Nat. Geosci.,* **6**(10), 852–855.

Bablon, M. *et al.* 2019. Interactions between volcanism and geodynamics in the southern termination of the Ecuadorian arc, *Tectonophysics,* **751,** 54–72.

Beauval, C. *et al.* 2013. An earthquake catalog for seismic hazard assessment in Ecuador, *Bull. seism. Soc. Am.,* **103**(2A), 773–786.

Calahorrano, A., Sallarès, V., Collot, J.Y., Sage, F. & Ranero, C.R., 2008. Nonlinear variations of the physical properties along the southern Ecuador subduction channel: results from depth-migrated seismic data, *Earth planet. Sci. Lett.,* **267**(3-4), 453–467.

Cardona, A. *et al.* 2011. Early-subduction-related orogeny in the northern Andes: turonian to eocene magmatic and provenance record in the Santa Marta Massif and Rancheria Basin, northern Colombia, *Terra Nova,* **23**(1), 26–34.

Chesley, C., Naif, S., Key, K. & Bassett, D., 2021. Fluid-rich subducting topography generates anomalous forearc porosity, *Nature,* **595**(7866), 255–260.

Chiaradia, M., Fontboté, L. & Paladines, A., 2004. Metal sources in mineral deposits and crustal rocks of Ecuador (1 N–4 S): a lead isotope synthesis, *Econ. Geol.,* **99**(6), 1085–1106.

Chiaradia, M., Müntener, O., Beate, B. & Fontignie, D., 2009. Adakite-like volcanism of Ecuador: lower crust magmatic evolution and recycling, *Contrib. Mineral. Petrol.,* **158,** 563–588.

Chlieh, M. *et al.* 2014. Distribution of discrete seismic asperities and aseismic slip along the Ecuadorian megathrust, *Earth planet. Sci. Lett.,* **400,** 292–301.

Christensen, N.I., 1996. Poisson's ratio and crustal seismology, *J. geophys. Res.: Solid Earth,* **101**(B2), 3139–3156.

Collot, J.Y. *et al.* 2004. Are rupture zone limits of great subduction earthquakes controlled by upper plate structures? Evidence from multichannel seismic reflection data acquired across the northern Ecuador–southwest Colombia margin, *J. geophys. Res.: Solid Earth,* **109**(B11), doi:10.1029/2004JB003060.

Collot, J.Y. *et al.* 2019. The Esmeraldas Canyon: a helpful marker of the pliocene-pleistocene tectonic deformation of the North Ecuador-Southwest Colombia convergent margin, *Tectonics,* **38**(8), 3140–3166.

Comte, D., Carrizo, D., Roecker, S., Ortega-Culaciati, F. & Peyrat, S., 2016. Three-dimensional elastic wave speeds in the northern Chile subduction zone: variations in hydration in the supraslab mantle, *Geophys. Suppl. Mon. Not. R. astr. Soc.,* **207**(2), 1080–1105.

Delph, J.R., Shimizu, K. & Ratschbacher, B.C., 2021. The architecture of the southern Puna magmatic system: integrating seismic and petrologic observations with geochemical modeling, *J. geophys. Res.: Solid Earth,* **126**(7), e2020JB021550, doi: 10.1029/2020JB021550.

Delph, J.R., Ward, K.M., Zandt, G., Ducea, M.N. & Beck, S.L., 2017. Imaging a magma plumbing system from MASH zone to magma reservoir, *Earth planet. Sci. Lett.,* **457,** 313–324.

Feininger, T., 1987. Allochthonous terranes in the Andes of Ecuador and northwestern Peru, *Can. J. Earth Sci.,* **24**(2), 266–278.

Font, Y., Segovia, M., Vaca, S. & Theunissen, T., 2013. Seismicity patterns along the Ecuadorian subduction zone: new constraints from earthquake

location in a 3-D *a priori* velocity model, *Geophys. J. Int.,* **193**(1), 263–286.

Gailler, A., Charvis, P. & Flueh, E.R., 2007. Segmentation of the Nazca and South American plates along the Ecuador subduction zone from wide angle seismic profiles, *Earth planet. Sci. Lett.,* **260**, 444–464.

Gallego, A., Russo, R.M., Comte, D., Mocanu, V.I., Murdie, R.E. & Vandecar, J.C., 2010. Seismic noise tomography in the Chile ridge subduction region, *Geophys. J. Int.,* **182**(3), 1478–1492.

George, S.W., Horton, B.K., Vallejo, C., Jackson, L.J. & Gutierrez, E.G., 2021. Did accretion of the Caribbean oceanic plateau drive rapid crustal thickening in the northern Andes?, *Geology,* **49**(8), 936–940.

Graindorge, D., Calahorrano, A., Charvis, P., Collot, J.Y. & Bethoux, N., 2004. Deep structures of the Ecuador convergent margin and the Carnegie Ridge, possible consequence on great earthquakes recurrence interval, *Geophys. Res. Lett.,* **31**(4), doi:10.1029/2003GL018803.

Guillier, B., Chatelain, J.L., Jaillard, E., Yepes, H., Poupinet, G. & Fels, J.F. 2001, Seismological evidence on the geometry of the orogenic system in central-northern Ecuador (South America), *Geophys. Res. Lett.,* **28**(19), 3749–3752.

Gutscher, M.A., Malavieille, J., Lallemand, S. & Collot, J.Y., 1999. Tectonic segmentation of the North Andean margin: impact of the Carnegie Ridge collision, *Earth planet. Sci. Lett.,* **168**(3-4), 255–270.

Gutscher, M.A., Spakman, W., Bijwaard, H. & Engdahl, E.R., 2000. Geodynamics of flat subduction: seismicity and tomographic constraints from the Andean margin, *Tectonics,* **19**(5), 814–833.

Hall, M. & Beate, B., 1991. El volcanismo Plio-Cuaternario en los Andes del Ecuador, ed. Mothes, P., *El Paisaje Volcánico de la Sierra Ecuatoriana, Estudios de Geografía* 4, Quito, 5–18.

Hall, M.L., Samaniego, P., Le Pennec, J.L. & Johnson, J.B., 2008. Ecuadorian Andes volcanism: a review of late pliocene to present activity, *J. Volc. Geotherm. Res.,* **176**(1), 1–6

Hardy, N.C., 1991. Tectonic evolution of the easternmost Panama Basin: some new data and inferences, *J. South Am. Earth Sci.,* **4**(3), 261–269.

Hayes, G.P., Moore, G.L., Portner, D.E., Hearne, M., Flamme, H., Furtney, M. & Smoczyk, G.M. 2018. Slab2, a comprehensive subduction zone geometry model, *Science,* **362**(6410), 58–61.

Hidalgo, S., Gerbe, M.C., Martin, H., Samaniego, P. & Bourdon, E., 2012. Role of crustal and slab components in the Northern Volcanic Zone of the Andes (Ecuador) constrained by Sr–Nd–O isotopes, *Lithos,* **132**, 180–192.

Hoskins, M.C. *et al.* 2021. Triggered crustal earthquake swarm across subduction segment boundary after the 2016 Pedernales, Ecuador megathrust earthquake, *Earth planet. Sci. Lett.,* **553**, 116620, doi: 10.1016/j.epsl.2020.116620.

Huangfu, P., Wang, Y., Cawood, P.A., Li, Z.H., Fan, W. & Gerya, T.V., 2016. Thermo-mechanical controls of flat subduction: insights from numerical modeling, *Gondwana Res.,* **40**, 170–183.

Hughes, R.A. & Pilatasig, L.F., 2002. Cretaceous and tertiary terrane accretion in the Cordillera Occidental of the Andes of Ecuador, *Tectonophysics,* **345**(1-4), 29–48.

IG-EPN, 2019. Instituto Geofísico Escuela Nacional Politecnica, Informe especial complejo volcánico Chiles–Cerro Negro n.1, August 2019.

Jaillard, E., Lapierre, H., Ordonez, M., Alava, J.T., Amortegui, A. & Vanmelle, J., 2009. Accreted oceanic terranes in Ecuador: southern edge of the Caribbean Plate?, *Geol. Soc. London, Special Publ.,* **328**(1), 469–485.

Kanamori, H. & McNally, K.C., 1982. Variable rupture mode of the subduction zone along the Ecuador-Colombia coast, *Bull. seism. Soc. Am.,* **72**(4), 1241–1253.

Kay, S.M. & Mpodozis, C., 2002. Magmatism as a probe to the Neogene shallowing of the Nazca plate beneath the modern Chilean flat-slab, *J. South Am. Earth Sci.,* **15**(1), 39–57.

Kendrick, E., Bevis, M., Smalley, R., Jr, Brooks, B., Vargas, R.B., Lauría, E. & Fortes, L.P.S., 2003. The Nazca–South America Euler vector and its rate of change, *J. South Am. Earth Sci.,* **16**(2), 125–131.

Kennett, B.L.N. & Engdahl, E.R. 1991. Traveltimes for global earthquake location and phase identification, *Geophys. J. Int.,* **105**(2), 429–465.

Kerr, A.C., Aspden, J.A., Tarney, J. & Pilatasig, L.F., 2002. The nature and provenance of accreted oceanic terranes in western Ecuador: geochemical and tectonic constraints, *J. Geol. Soc.,* **159**(5), 577–594.

Koch, C.D. *et al.* 2020. Structure of the Ecuadorian forearc from the joint inversion of receiver functions and ambient noise surface waves, *Geophys. J. Int.,* **222**(3), 1671–1685.

Koch, C.D. *et al.* 2021. Crustal thickness and magma storage beneath the Ecuadorian arc, *J. South Am. Earth Sci.,* **110**, 103331, doi:10.1016/j.jsames.2021.103331.

Koulakov, I., Sobolev, S.V. & Asch, G., 2006. *P*-and *S*-velocity images of the lithosphere—Asthenosphere system in the Central Andes from local-source tomographic inversion, *Geophys. J. Int.,* **167**(1), 106–126.

Lay, T., Kanamori, H., Ammon, C.J., Koper, K.D., Hutko, A.R., Ye, L., Yue, H. & Rushing, T.M., 2012. Depth-varying rupture properties of subduction zone megathrust faults, *J. geophys. Res.: Solid Earth,* **117**(B4), doi:10.1029/2011JB009133.

Lebrat, M., Mégard, F., Dupuy, C. & Dostal, J., 1987. Geochemistry of the cretaceous volcanic rocks of Ecuador: geodynamic implications, *Bull. Geol. Soc. Am,* **22**, doi:10.1130/0016-7606(1987)99<569:GATSOP>2.0.CO;2.

Leon-Rios, S. *et al.* 2019. 1D-velocity structure and seismotectonics of the Ecuadorian margin inferred from the 2016 M_w7.8 Pedernales aftershock sequence, *Tectonophysics,* **767**, 228165, doi:10.1016/j.tecto.2019.228165.

León-Ríos, S. *et al.* 2021. 3D local earthquake tomography of the Ecuadorian margin in the source area of the 2016 M_w 7.8 Pedernales earthquake, *J. geophys. Res.: Solid Earth,* **126**(3), e2020JB020701, doi: 10.1029/2020JB020701.

Li, Z., Roecker, S., Zhihai, L., Bin, W., Haitao, W., Schelochkov, G. & Bragin, V., 2009. Tomographic image of the crust and upper mantle beneath the western Tien Shan from the MANAS broadband deployment: possible evidence for lithospheric delamination, *Tectonophysics,* **477**(1-2), 49–57.

Liu, Y. & Rice, J.R., 2007. Spontaneous and triggered aseismic deformation transients in a subduction fault model, *J. geophys. Res.: Solid Earth,* **112**(B9), doi:10.1029/2007JB004930.

Löbens, S., Bense, F.A., Wemmer, K., Dunkl, I., Costa, C.H., Layer, P. & Siegesmund, S., 2011. Exhumation and uplift of the Sierras Pampeanas: preliminary implications from K–Ar fault gouge dating and low-T thermochronology in the Sierra de Comechingones (Argentina), *Int. J. Earth Sci.,* **100**, 671–694.

Lonsdale, P., 2005, Creation of the Cocos and Nazca plates by fission of the Farallon plate, *Tectonophysics,* **404**(3-4), 237–264.

Luzieux, L.D.A., Heller, F., Spikings, R., Vallejo, C.F. & Winkler, W., 2006. Origin and cretaceous tectonic history of the coastal Ecuadorian forearc between 1 N and 3 S: paleomagnetic, radiometric and fossil evidence, *Earth planet. Sci. Lett.,* **249**(3-4), 400–414.

Lynner, C. *et al.* 2020. Upper-plate structure in Ecuador coincident with the subduction of the Carnegie Ridge and the southern extent of large mega-thrust earthquakes, *Geophys. J. Int.,* **220**(3), 1965–1977.

Lynner, C., Beck, S.L., Zandt, G., Porritt, R.W., Lin, F.C. & Eilon, Z.C., 2018. Midcrustal deformation in the Central Andes constrained by radial anisotropy, *J. geophys. Res.: Solid Earth,* **123**(6), 4798–4813.

Mamberti, M., Lapierre, H., Bosch, D., Jaillard, E., Ethien, R., Hernandez, J. & Polvé, M., 2003. Accreted fragments of the late cretaceous Caribbean–Colombian Plateau in Ecuador, *Lithosphere,* **66**(3-4), 173–199.

Marcaillou, B., Collot, J.Y., Ribodetti, A., d'Acremont, E., Mahamat, A.A. & Alvarado, A., 2016. Seamount subduction at the North-Ecuadorian convergent margin: effects on structures, inter-seismic coupling and seismogenesis, *Earth planet. Sci. Lett.,* **433**, 146–158.

Margirier, A., Strecker, M.R., Reiners, P.W., Thomson, S.N., Casado, I., George, S.W. & Alvarado, A., 2023. Late Miocene exhumation of the Western Cordillera, Ecuador, driven by increased coupling between the subducting Carnegie Ridge and the South American continent, *Tectonics,* **42**(1), e2022TC007344, doi: 10.1029/2022TC007344.

Martel, C., Andújar, J., Mothes, P., Scaillet, B., Pichavant, M. & Molina, I., 2018. Storage conditions of the mafic and silicic magmas at Cotopaxi, Ecuador, *J. Volc. Geotherm. Res.,* **354,** 74–86.

McCourt, W.J., Duque, P., Pilatasig, L.F. & Villagómez, R., 1998. Mapa geológico de la Cordillera Occidental del Ecuador entre 1-2 S., escala 1/200.000, CODIGEM-Min. *Energ. Min. BGS publs.,* Quito.

Meltzer, A. *et al.* 2019. The 2016 M_w 7.8 Pedernales, Ecuador, earthquake: rapid response deployment, *Seismol. Res. Lett.,* **90**(3), 1346–1354.

Michaud, F., Witt, C. & Royer, J.Y., 2009. Influence of the subduction of the Carnegie volcanic ridge on Ecuadorian geology: reality and fiction, in *Backbone of the Americas: Shallow Subduction, Plateau Uplift, and Ridge and Terrane Collision, Vol. 204,* pp. 217, eds Kay, S. M., Ramos, V. A. & Dickinson, W. R., Geological Society of America.

Miura, S., Suyehiro, K., Shinohara, M., Takahashi, N., Araki, E. & Taira, A., 2004, Seismological structure and implications of collision between the Ontong Java Plateau and Solomon Island Arc from ocean bottom seismometer-airgun data, *Tectonophysics,* **389**(3–4), 191–220.

Montagner, J.P., 1986. Regional three-dimensional structures using long-period surface waves, *Ann. Geophys,,* **4(B3)** 283–294

Moreno, M. *et al.* 2018. Chilean megathrust earthquake recurrence linked to frictional contrast at depth, *Nat. Geosci.,* **11**(4), 285–290.

Müller, R.D., Sdrolias, M., Gaina, C. & Roest, W.R., 2008. Age, spreading rates, and spreading asymmetry of the world's ocean crust, *Geochem. Geophys. Geosyst.,* **9**(4), doi:10.1029/2007GC001743.

NEIC Earthquake catalogue, 2023. National Earthquake Information Centre, On-line Bulletin, http://earthquake.usgs.gov/earthquakes/search/. (Last accessed 31 March 2023).

Nocquet, J.M. *et al.* 2014. Motion of continental slivers and creeping subduction in the northern Andes, *Nat. Geosci.,* **7**(4), 287–291.

Nocquet, J.M. *et al.* 2017. Supercycle at the Ecuadorian subduction zone revealed after the 2016 Pedernales earthquake, *Nat. Geosci.,* **10**(2), 145–149.

Nunn, C., Roecker, S.W., Priestley, K.F., Liang, X. & Gilligan, A., 2014. Joint inversion of surface waves and teleseismic body waves across the Tibetan collision zone: the fate of subducted Indian lithosphere, *Geophys. J. Int.,* **198**(3), 1526–1542.

Operto, S. & Charvis, P., 1996. Deep structure of the southern Kerguelen Plateau (southern Indian Ocean) from ocean bottom seismometer wide-angle seismic data, *J. geophys. Res.: Solid Earth,* **101**(B11), 25 077–25 103.

Paige, C.C. & Saunders, M. A., 1982. LSQR: An Algorithm for Sparse Linear Equations and Sparse Least Squares, *ACM Transactions on Mathematical Software,* **8** (1), 43, doi:10.1145/355984.355989.

Pavlis, G.L. & Vernon, F.L., 2010. Array processing of teleseismic body waves with the USArray, *Comput. Geosci.,* **36**(7), 910–920.

Portner, D.E. *et al.* 2020. Detailed structure of the subducted Nazca slab into the lower mantle derived from continent-scale teleseismic *P* wave tomography, *J. geophys. Res.: Solid Earth,* **125**(5), e2019JB017884, doi: 10.1029/2019JB017884.

Poveda, E., Monsalve, G. & Vargas, C.A., 2015. Receiver functions and crustal structure of the northwestern Andean region, Colombia, *J. geophys. Res.: Solid Earth,* **120**(4), 2408–2425.

Ramos, V.A. & Folguera, A., 2009. Andean flat-slab subduction through time, *Geol. Soc. London, Special Publ.,* **327**(1), 31–54.

Régnier, M., Font, Y., Charvis, P., Mercerat, D., Rietbrock, A., Ruiz, M. & Alvarado, A., 2016. *Pedernales [Data set].* International Federation of Digital Seismograph Networks..

Rodríguez, E.E. *et al.* 2021. Mantle dynamics of the Andean Subduction Zone from continent-scale teleseismic *S*-wave tomography, *Geophys. J. Int.,* **224**(3), 1553–1571.

Rodríguez, E.E. *et al.* 2024 Seismic imaging of the northern andean subduction zone from teleseismic tomography: a torn and fragmented Nazca slab, *Geophys. J. Int.,* **236,** 593–606.

Roecker, S. *et al.* 2017. Subsurface images of the Eastern Rift, Africa, from the joint inversion of body waves, surface waves and gravity: investigating the role of fluids in early-stage continental rifting, *Geophys. J. Int.,* **210**(2), 931–950, doi: 10.1093/gji/ggx220.

Roecker, S., Thurber, C. & McPhee, D., 2004. Joint inversion of gravity and arrival time data from Parkfield: new constraints on structure and hypocenter locations near the SAFOD drill site, *Geophys. Res. Lett.,* **31**(12), doi:10.1029/2003GL019396.

Roecker, S., Thurber, C., Roberts, K. & Powell, L., 2006. Refining the image of the San Andreas Fault near Parkfield, California using a finite difference travel time computation technique, *Tectonophysics,* **426**(1-2), 189–205, doi:10.1016/j.tecto.2006.02.026.

Rolandone, F. *et al.* 2018. Areas prone to slow slip events impede earthquake rupture propagation and promote afterslip, *Sci. Adv.,* **4**(1), eaao6596, doi: 10.1126/sciadv.aao6596.

Rosenbaum, G., Sandiford, M., Caulfield, J. & Garrison, J.M., 2019. A trapdoor mechanism for slab tearing and melt generation in the northern Andes, *Geology,* **47**(1), 23–26.

Ruiz, M. 2016. Ecuador RENSIG data, *Data Services Newsletter,* **18**(2). https://ds.iris.edu/ds/newsletter/vol18/no2/467/ecuador-rensig-data.

Saalfeld, M.A., Kelley, D.F. & Panter, K.S., 2019. Insight on magma evolution and storage through the recent eruptive history of Cotopaxi Volcano, Ecuador, *J. South Am. Earth Sci.,* **93,** 85–101.

Sallarès, V. & Charvis, P., 2003. Crustal thickness constraints on the geodynamic evolution of the Galapagos Volcanic Province, *Earth planet. Sci. Lett.,* **214**(3-4), 545–559.

Samaniego, P., Martin, H., Monzier, M., Robin, C., Fornari, M., Eissen, J.P. & Cotten, J., 2005. Temporal evolution of magmatism in the Northern Volcanic Zone of the Andes: the geology and petrology of Cayambe Volcanic Complex (Ecuador), *Journal of petrology,* **46**(11), 2225–2252.

Samaniego, P., Robin, C., Chazot, G., Bourdon, E. & Cotten, J., 2010. Evolving metasomatic agent in the Northern Andean subduction zone, deduced from magma composition of the long-lived Pichincha volcanic complex (Ecuador), *Contrib. Mineral. Petrol.,* **160,** 239–260.

Schurr, B., Rietbrock, A., Asch, G., Kind, R. & Oncken, O., 2006. Evidence for lithospheric detachment in the central Andes from local earthquake tomography, *Tectonophysics,* **415**(1-4), 203–223.

Schütte, P., Chiaradia, M. & Beate, B., 2010. Geodynamic controls on tertiary arc magmatism in Ecuador: constraints from U–Pb zircon geochronology of oligocene–Miocene intrusions and regional age distribution trends, *Tectonophysics,* **489**(1-4), 159–176.

Segovia, M. *et al.* 2018. Seismicity distribution near a subducting seamount in the Central Ecuadorian subduction zone, space-time relation to a slow-slip event, *Tectonics,* **37**(7), 2106–2123.

Servicio Geológico Colombiano, 1993. *Red Sismologica Nacional de Colombia [Data set].* International Federation of Digital Seismograph Networks. https://www.sgc.gov.co/

Seton, M. *et al.* 2020. A global data set of present-day oceanic crustal age and seafloor spreading parameters, *Geochem. Geophys. Geosyst.,* **21**(10), e2020GC009214, doi: 10.1029/2020GC009214.

Siebert, L., Simkin, T. & Kimberly, P., 2011. *Volcanoes of the World,* University of California Press.

Soto-Cordero, L. *et al.* 2020. Structural control on megathrust rupture and slip behavior: insights from the 2016 M_w 7.8 Pedernales Ecuador earthquake, *J. geophys. Res.: Solid Earth,* **125**(2), e2019JB018001, doi: 10.1029/2019JB018001.

Spikings, R.A. & Crowhurst, P.V., 2004. (U–Th)/He thermochronometric constraints on the late miocene–Pliocene tectonic development of the northern Cordillera Real and the Interandean Depression, Ecuador, *J. South Am. Earth Sci.,* **17**(4), 239–251.

Spikings, R.A., Crowhurst, P.V., Winkler, W. & Villagomez, D., 2010. Syn-and post-accretionary cooling history of the Ecuadorian Andes constrained by their in-situ and detrital thermochronometric record, *J. South Am. Earth Sci.,* **30**(3-4), 121–133.

Swenson, J.L. & Beck, S.L., 1999. Source characteristics of the 12 November 1996 M w 7.7 Peru subduction zone earthquake. Seismogenic and tsunamigenic processes in shallow subduction zones, 731–751,.

Syracuse, E.M., Maceira, M., Prieto, G.A., Zhang, H. & Ammon, C.J., 2016. Multiple plates subducting beneath Colombia, as illuminated by

seismicity and velocity from the joint inversion of seismic and gravity data, *Earth planet. Sci. Lett.,* **444,** 139–149.

Trenkamp, R., Kellogg, J.N., Freymueller, J.T. & Mora, H.P., 2002. Wide plate margin deformation, southern Central America and northwestern South America, CASA GPS observations, *J. South Am. Earth Sci.,* **15**(2), 157–171.

Vaca, S., Vallée, M., Nocquet, J.M., Battaglia, J. & Régnier, M., 2018. Recurrent slow slip events as a barrier to the northward rupture propagation of the 2016 Pedernales earthquake (Central Ecuador), *Tectonophysics,* **724,** 80–92.

Vallée, M. *et al.* 2013. Intense interface seismicity triggered by a shallow slow slip event in the Central Ecuador subduction zone, *J. geophys. Res.: Solid Earth,* **118**(6), 2965–2981.

Vallejo, C., Soria, F., Tornos, F., Naranjo, G., Rosero, B., Salazar, F. & Cochrane, R., 2016. Geology of El Domo deposit in central Ecuador: a VMS formed on top of an accreted margin, *Miner. Deposita,* **51,** 389–409.

Vallejo, C., Spikings, R.A., Horton, B.K., Luzieux, L., Romero, C., Winkler, W. & Thomsen, T.B., 2019. Late cretaceous to miocene stratigraphy and provenance of the coastal forearc and Western Cordillera of Ecuador: evidence for accretion of a single oceanic plateau fragment, in *Andean Tectonics,* pp. 209–236, Elsevier.

VanDecar, J.C. & Crosson, R.S., 1990. Determination of teleseismic relative phase arrival times using multi-channel cross-correlation and least squares, *Bull. seism. Soc. Am.,* **80**(1), 150–169.

Villegas-Lanza, J.C., Chlieh, M., Cavalié, O., Tavera, H., Baby, P., Chire-Chira, J. & Nocquet, J.M., 2016. Active tectonics of Peru: heterogeneous interseismic coupling along the Nazca megathrust, rigid motion of the Peruvian sliver, and Subandean shortening accommodation, *J. geophys. Res.: Solid Earth,* **121**(10), 7371–7394.

Ward, K.M., Porter, R.C., Zandt, G., Beck, S.L., Wagner, L.S., Minaya, E. & Tavera, H., 2013. Ambient noise tomography across the Central Andes, *Geophys. J. Int.,* **194**(3), 1559–1573.

Witt, C., Bourgois, J., Michaud, F., Ordonez, M., Jime´nez, N. & Sosson, M. 2006. Development of the Gulf of Guayaquil (Ecuador) during the Quaternary as an effect of the North Andean block tectonic escape, *Tectonics,* **25,** TC3017, doi: 10.1029/2004TC001723.

Worthington, L.L., Van Avendonk, H.J., Gulick, S.P., Christeson, G.L. & Pavlis, T.L., 2012. Crustal structure of the Yakutat terrane and the evolution of subduction and collision in southern Alaska, *J. geophys. Res.: Solid Earth,* **117**(B1), doi:10.1029/2011JB008493.

Yáñez, G.A., Ranero, C.R., von Huene, R. & Díaz, J., 2001. Magnetic anomaly interpretation across the southern central Andes (32–34 S): the role of the Juan Fernández Ridge in the late tertiary evolution of the margin, *J. geophys. Res.: Solid Earth,* **106**(B4), 6325–6345.

Yepes, H., Audin, L., Alvarado, A., Beauval, C., Aguilar, J., Font, Y. & Cotton, F., 2016. A new view for the geodynamics of Ecuador: implication in seismogenic source definition and seismic hazard assessment, *Tectonics,* **35**(5), 1249–1279.

Zhang, H., Roecker, S., Thurber, C.H., Wang, W. & Dar, I.A., 2012. Seismic imaging of microblocks and weak zones in the crust beneath the southeastern margin of the Tibetan Plateau, *Earth Sciences,* 159–202, doi:10.5772/27876.